Numerical Transfer Matrix Method of Next-nearest-neighbor Ising Models

by

Yi Hu

Department of Computer Science
Duke University

Date: _____

Approved:

_____
Sayan Mukherjee, Advisor

_____
Patrick Charbonneau

_____
Raluca Gordân

Thesis submitted in partial fulfillment of the requirements for the degree of
Master of Science in the Department of Computer Science
in the Graduate School of Duke University
2021

Abstract

Numerical Transfer Matrix Method of Next-nearest-neighbor Ising Models

by

Yi Hu

Department of Computer Science
Duke University

Date: _____

Approved:

_____
Sayan Mukherjee, Advisor

_____
Patrick Charbonneau

_____
Raluca Gordân

An abstract of a thesis submitted in partial fulfillment of the requirements for the degree of Master of Science in the Department of Computer Science in the Graduate School of Duke University
2021

Copyright © 2021 by Yi Hu
All rights reserved except the rights granted by the
Creative Commons Attribution-Noncommercial Licence

Abstract

In statistical physics, the exact partition function of simple (quasi)-one-dimensional models can be obtained from the numerical transfer matrix (TM) method. This method involves solving for the leading eigenvalues of a matrix representing all possible interactions between the states that a unit of the system can take. Because the size of this matrix grows exponentially with the number of those units, the TM method is ideally suited for models that have a finite state space and short-range interactions. Its success nevertheless relies on the use of efficient iterative eigensolvers and on leveraging system symmetry, whenever possible.

By careful finite-size extrapolation of sufficiently large systems, the TM method can also be used to examine two-dimensional models. A particularly interesting series of such systems are Ising models modified with next-nearest-neighbor frustration, which recapitulate the formation of equilibrium modulated phases in systems as varied as magnetic alloys, lipid surfactants, and cell morphogenesis. In these models, frustration results in large mixing times for Markov chain Monte Carlo simulations, but the TM approach sidesteps this slowdown and thus provides a putatively well-controlled computational scheme. The effectiveness of TM approach for these models, however, had previously been obfuscated by the limited range of system sizes computationally available for the numerical analysis.

In this thesis, I build on the sparse matrix decomposition and take advantage of the structure and symmetry of the TM to develop optimized algorithms for the

method, and thereby overcome the computational challenge. The resulting algorithm is implemented in various canonical frustrated next-nearest-neighbor Ising models, aiming to solve long-standing physical problems in these models. The approach provides benchmark results for related statistical physics models. It could also inspire the development of adapted eigensolver for similarly structured matrices.

Contents

Abstract **iv**

List of Figures **ix**

List of Abbreviations and Symbols **xi**

1 Introduction **1**

1.1 Outline 2

1.2 Physical background 3

1.2.1 Model definition 4

1.2.2 Thermodynamics overview 6

1.3 Iterative eigenvalue algorithms 7

1.3.1 Power iteration 8

1.3.2 Arnoldi iteration 8

1.3.3 Implicitly restarted Arnoldi method and ARPACK 9

2 Transfer matrix method **10**

2.1 Decomposition for the matrix-vector multiplication 11

2.1.1 ANNNI model propagated perpendicular to the axial direction 11

2.1.2 ANNNI model propagated along the axial direction 15

2.1.3 DNNI Model 16

2.1.4 BNNNI Model and 3NNI model 18

2.2 Reducing space complexity with symmetry 20

2.2.1 General case 20
2.2.2 $_{\perp}$TM and $_{/}$TM 23
2.2.3 $_{\parallel}$TM 26
2.2.4 Remarks 28
2.3 Planting configurations via transfer matrices 29
2.3.1 General case 29
2.3.2 Compressed transfer matrices 31
3 Physical property investigation **32**
3.1 ANNNI model 32
3.1.1 Overview 32
3.1.2 Signatures on incommensurability 33
3.1.3 Phase diagram for $h = 0$ 36
3.1.4 Phases diagram for $h > 0$ 42
3.2 DNNI model 44
3.2.1 Overview 44
3.2.2 Thermodynamic Observables 45
3.2.3 T_{c} determination 46
3.2.4 Order of transition 47
3.3 BNNNI model 52
3.3.1 Overview 52
3.3.2 Correlation length scaling 52
3.3.3 Heat capacity evolution 55
3.3.4 Phase diagram 56
3.4 3NNI model 58
3.4.1 Overview 58

3.4.2 Melting of antiphases 59
3.4.3 Phase diagram for $\kappa = \kappa'/2$ 60
4 Conclusions **63**
Bibliography **65**

List of Figures

1.1 Schematics of (a) ANNNI, (b) DNNI, (c) BNNNI and (d) 3NNI models 4

2.1 Schematics of inter-layer interactions in different TM approaches . . . 12

2.2 Number of equivalent state sets (m) of different symmetry group grows with layer length (L) in (left) $_{\perp}$TM and (right) $_{\parallel}$TM 24

3.1 Leading correlation length for the ANNNI model with $\kappa = 0.6$ in $_{\perp}$TM and $_{\parallel}$TM 34

3.2 Domain wall free energy $\tau_L^{(+/-)}(T)$ for the ANNNI model with $\kappa = 0.6$ from $_{\perp}$TM 35

3.3 Thermodynamic and structural observables of the ANNNI model from $_{\perp}$TM 37

3.4 Correlation length analysis for the ANNNI model from $_{\parallel}$TM 40

3.5 Phase diagram for the two-dimensional ANNNI model with $h = 0$ . . 41

3.6 Phase diagram for the two-dimensional ANNNI model with $\kappa = 0.6$ and varying h 43

3.7 Finite-size results for various observables of the DNNI model with $\kappa = 0.6$ 45

3.8 Phase transition determination for the DNNI model around $\kappa = 1/2$. 46

3.9 Finite-size scaling of the DNNI peak specific heat for various κ 48

3.10 The DNNI model exhibits pronounced pre-asymptotic corrections around $\kappa = 1/2$ 50

3.11 $T = 0$ (ground state) phase diagram for the 3NNI model 51

3.12 Leading correlation length for the BNNNI model with $\kappa = 0.6$ in $_{\parallel}$TM and $_{/}$TM 53

3.13 Specific heat for the BNNNI model for $\kappa = 0.6$ in $_{\|}$TM and $_{/}$TM . . . 56

3.14 Phase diagram for the BNNNI model 57

3.15 Correlation length scaling of the 3NNI model for different frustration parameters 60

3.16 Phase diagram for the 3NNI model for $\kappa = \kappa'/2$ 61

List of Abbreviations and Symbols

Symbols

α	Specific heat exponent
β	Inverse temperature
κ, κ'	Frustration strengths
λ_0, λ_1, ...	Leading and subleading eigenvalues
$\mathbf{\Lambda}$	Matrix of eigenvalues in eigendecomposition
ν	Correlation length exponent
θ	Anisotropic exponent
$\tau^{(+/-)}$	Domain wall free energy
φ_0, φ_1, ...	Leading and subleading eigenvectors
ξ_1, ξ_2, ...	Leading and subleading correlation lengths
a	Layer configuration indices
$[b]$	Equivalent layer configuration indices
c	specific heat
C_n, C_{nv}	Cyclic groups
D_{nh}	Dihedral groups
h	External field strength
$\mathbf{H}$	Hessenberg matrix
$\mathcal{H}$	Hamiltonian
L	Layer length, i.e., strip width

J	Coupling constant
$\mathbf{M}$	Compressed transfer matrix
N	Strip length ($\to \infty$)
N_{states}	Number of states
N_{mod}	Number of modulation layer
netp	Net positive spin
$\mathcal{O}(\cdot)$	Order of
$P(\cdot)$, $P(\cdot\|\cdot)$	Marginal and conditional probabilities
$Q(\cdot)$, $Q(\cdot\|\cdot)$	Cumulative marginal and conditional probabilities
$\mathbf{Q}$	Matrix of eigenvectors in eigendecomposition
rol	Bit rotate left shift
ror	Bit rotate right shift
q	Modulation wavenumber
s	Spin
$\mathbf{s}$	Spin layer configuration as vector
tr	Matrix trace
T	Temperature
T_{c}, T_{c1}, T_{c2}	Phase transition temperatures
$\mathbf{T}$	Transfer matrix
u	internal energy per spin
V_x, V_z	Intra-layer and inter-layer interaction
Y_L	Correlation length local exponent
Z_L	Modulation wavenumber local exponent

Abbreviations

3NNI	Third-nearest-neighbor Ising (model)
ANNNI	Axial next-nearest-neighbor Ising (model)
ARPACK	Arnoldi package
AT	Ashkin-Teller (transition)
BNNNI	Bixial next-nearest-neighbor Ising (model)
DMRG	Density matrix renormalization group
DNNI	Diagonal nearest-neighbor Ising (model)
IC	Incommensurate
KT	Kosterlitz-Thouless (transition)
SALR	Short-range attraction and long-range repulsion
TM	Transfer matrix
$_{\perp}$TM, $_{\parallel}$TM, $_{/}$TM	Transfer matrices propagated perpendicular to, in parallel with, diagonal to the direction of next-nearest-neighbor interaction

1

Introduction

Determining the eigenvalues of a matrix is a traditional numerical analysis problem, which has broad applications in contemporary science and engineering [1]. Because, in practice, one often only needs to solve for a few edge eigenvalues from a large matrix, various iterative eigensolvers have been developed for this purpose—from the simplest power iteration, QR iteration, the family of Krylov subspace based methods [2–5] to inexact methods [6–8]. Efficient and stable iterative eigensolvers have thus been developed for both general purposes and specific applications. In the latter case, significant computational gains over generic approaches can be achieved by utilizing the structure of the problem and the demand for accuracy. For example, the density matrix renormalization group (DMRG) approach to quantum chemistry problems [9–11] employs a physics-motivated ansatz on the eigenvector to significantly reduce the size of the problem.

In statistical physics, eigensolvers are commonly used for solving models using the transfer matrix (TM) method. This scheme expresses the partition function of simple models in low (physical) dimension as a product of matrices, and in the thermodynamic limit (which corresponds to raising the matrix product to infinity)

the leading eigenvalue of the TM gives the exact partition function of the model. First introduced by Kramers and Wannier in 1940s [12], this method has since played a key role in obtaining exact and sometimes even analytical solutions of many reference models [13, 14]. In particular, the TM approach is commonly applied to Ising-like models.

Recall that a simple Ising model consists of classical spin variables that take two discrete states ($s \in \{+1, -1\}$) located at each node of a lattice, with each spin interacting pairwise with its nearest (edge-sharing) neighbors. Also, an external (magnetic) field are sometimes applied. The model is one of the minimal systems to display a macroscopic phase transition, which makes it central to the study of condensed matter. Variants of this model have found applications in a variety of contexts. For example, spin glass models (e.g. Edwards-Anderson and Sherrington-Kirkpatrick models) are not only key to the physics of disordered materials, but are also intimately linked to the theory of neural networks [15]. Ising models are also closely related to fundamental graph theory problems in computer science. For instance, the max-cut problem is equivalent to the energy minimization on an anti-ferromagnetic Ising model [16], and the max-flow min-cut problem can be mapped on a ferromagnetic Ising model with local external field as well. Therefore, developments of statistical physics methods and computer science algorithms share much and mutually benefit [17].

1.1 Outline

In this thesis, I introduce the numerical transfer matrix method for a family of next-nearest-neighbor Ising models. As a systematic recapitulation and extension of earlier studies [18–22], I describe the implementation of efficient algorithms to study the statistical physics of these models. In the remainder of the introduction, I physically motivate the study of this class of model, then define the specific models of

interest, before introducing key aspects of iterative eigenvalue algorithms that will be useful for later discussion. Chapter 2 details the algorithms and their expected time and space complexity. Physical results obtained by the TM approach are presented in Chap. 3, and a brief summary and outlook are provided in Chap. 4.

1.2 Physical background

The consideration of next-nearest-neighbor Ising models is motivated by the study of ordered modulated phases such as shown in Fig. 1.1. These phases notably form in systems whose components interact with competing short-range attraction and long-range repulsion (SALR) [23, 24], which appear in materials as varied as magnetic alloys, lipid surfactants, and biological tissues. Frustration, however, gives rise to slowly decaying correlations and complex relaxation processes in the disordered regime, which can interfere with the formation of ordered patterns. The problem also arises in numerical simulations. Existing simulation techniques often fail to surmount these difficulties in even minimal microphase-forming models. In this context, the mastery minimal models can be especially useful for establishing benchmarks for computational method development, and as stepping stones towards the study of richer systems.

Simple lattice SALR models have been studied since the 1980s, including the axial nearest-neighbor Ising (ANNNI), biaxial nearest-neighbor Ising (BNNNI) and diagonal nearest-neighbor Ising (DNNI) (also called J_1-J_2 model) model. As their names suggest, these models are decorated versions of the simple Ising model with different types of longer-range frustration (Figure 1.1). Despite the apparent simplicity of these models, certain aspects of their phase behavior remains debated. For instance, it is still unclear if the two-dimensional ANNNI model [25], which shows a modulated phase at low to intermediate temperatures when frustration is sufficiently strong, exhibits a "floating" (or incommensurate) layered phase or not [26–28]. Even

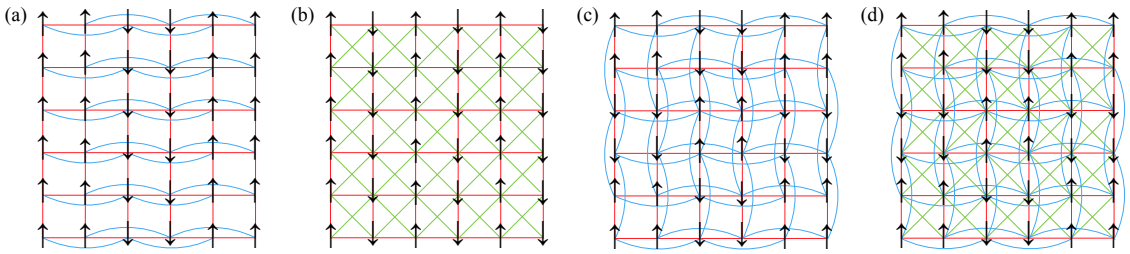

FIGURE 1.1: Schematics of (a) ANNNI, (b) DNNI, (c) BNNNI and (d) 3NNI models. Arrows denote spins; red, green and blue lines denote the nearest-neighbor, diagonal and axial next-nearest-neighbor interactions, respectively.

numerical simulations of very large systems do not provide a clear resolution [27].

It was quickly realized that these ambiguities could formally be surmounted by coupling a TM approach with a finite-size scaling analysis [18–20], but the extraction of relevant physical insight has long been hindered by computational limitations. The problem is that the TM solutions were obtained for strips of finite width L that were too small for the finite-size scaling analysis to extrapolate reliably to the thermodynamic limit, $L \to \infty$. Given the exponential growth of algorithmic complexity of TM with L, the large pre-asymptotic corrections frustrated models exhibit, and the limited computational resources then available, this obfuscation is somewhat unsurprising. The exponential improvement of computational resources over the years (Moore's Law) and the emergence of more efficient eigensolvers [4] nevertheless offer hope that the situation might have improved since. For instance, TM now provide insight into fairly complex (quasi-)one-dimensional systems [29–33]. Two-dimensional next-nearest-neighbor Ising models thus appear within reach, as I demonstrate for various examples in this thesis.

1.2.1 Model definition

The specific models I consider are as follows.

1. ANNNI Model.

The ANNNI model is a minimal model for microphase-forming systems with modulated phases in equilibrium. The Hamiltonian reads

$$\mathcal{H}_{\mathrm{ANNNI}} = -J \sum_{\langle i,j \rangle} s_i s_j + \kappa J \sum_{\langle i,j \rangle_{\mathrm{ANNN}}} s_i s_j - h \sum_i s_i, \tag{1.1}$$

where spin variables $s_i = \pm 1$, coupling constant $J > 0$ (and we scale $J = 1$ throughout this work), frustration strength of axial next-nearest-neighbor direction $\kappa > 0$ and external field h. When $\kappa = 0$ it reduces the standard Ising model.

2. DNNI Model.

   The DNNI model can be viewed as a modified Ising model where the diagonal nearest-neighbor interaction is included. The Hamiltonian reads

$$\mathcal{H}_{\mathrm{DNNI}} = -J \sum_{\langle i,j \rangle} s_i s_j + \kappa J \sum_{\langle i,j \rangle_{\mathrm{DNN}}} s_i s_j - h \sum_i s_i, \tag{1.2}$$

   with same parameter settings to the ANNNI model.

3. BNNNI model and 3NNI models.

   Including biaxial next-nearest-neighbor interactions, i.e., couplings with Euclidean third-nearest-neighbor (3NN), gives rise to the 3NNI Ising model (also known as the J_1-J_2-J_3 Ising model [34]). Its Hamiltonian reads

$$\mathcal{H}_{\mathrm{3NNI}} = -J \sum_{\langle i,j \rangle} s_i s_j + \kappa J \sum_{\langle i,j \rangle_{\mathrm{BNNN}}} s_i s_j + \kappa' J \sum_{\langle i,j \rangle_{\mathrm{DNN}}} s_i s_j - h \sum_i s_i, \tag{1.3}$$

   Setting $\kappa' = 0$ reduces that expression to that of the biaxial next-nearest-neighbor Ising (BNNNI) model.

1.2.2 Thermodynamics overview

Having defined the Hamiltonians for these models we can then construct their TM representations and solve for the thermodynamics. Generically, TMs encode the interaction between subsequent layers,

$$\mathbf{T}_{a,a'} = \exp[-\beta(V_x(a) + V_z(a, a'))], \tag{1.4}$$

where $\beta = 1/k_B T$ is the inverse temperature (the Boltzmann constant is set to unity, $k_B = 1$), a, a' denote subsequent layer spin states, and V_x and V_z are intra- and inter-layer interaction energies. The partition function of the strip of length N is given by $\mathrm{tr}\left(\mathbf{T}^N\right)$, and in the limit of $N \to \infty$, Z is given by the leading eigenvalue of $\mathbf{T}^N$, λ_0^N. The free energy per spin is thus

$$\beta f = -\frac{\ln \lambda_0}{L}, \tag{1.5}$$

and the marginal probability of a state a is given by the product of (normalized) left and right eigenvector of λ_0, $P(a) = \varphi_0^{-1}(a)\varphi_0(a)$ (after normalizing as $\sum_a P(a) = 1$). Given the leading eigenvalue and eigenvector, thermodynamic observables can be obtained exactly, including the internal energy per spin, $\beta u = -\partial(\beta f)/\partial T$, and the specific heat per spin, $c = \partial u/\partial T$.

One of the key advantages of TMs is that they also provide the correlation length ξ, which is important for identifying the location and nature of phase transitions. Given that the conditional probability of finding a subsequent layer state a' after layer a is [33]

$$P(a'|a) = \frac{\mathbf{T}_{a,a'}\varphi_0(a')}{\lambda_0 \varphi_0(a)}, \tag{1.6}$$

the generic conditional probability for a' having distances N from a is then

$$P^{(N)}(a'|a) = \frac{\mathbf{T}^N_{a,a'}\varphi_0(a')}{\lambda_0^N\varphi_0(a)} = P(a') + \sum_{i=1}^{|\{a\}|-1}\left(\frac{\lambda_i}{\lambda_0}\right)^N \frac{\varphi_i(a)\varphi_i^{-1}(a')\varphi_0(a')}{\varphi_0(a)}, \tag{1.7}$$

$$P^{(N)}(a'|a) - P(a') \sim \exp\left[N\ln\left(\frac{|\lambda_1|}{\lambda_0}\right)\right] = \exp(-N/\xi_1),$$

where $|\{a\}|$ is the total number of states and $\xi_1 = -1/\ln(|\lambda_1|/\lambda_0)$ is the leading correlation length.

1.3 Iterative eigenvalue algorithms

The numerical TM method used in this thesis is based on open-source iterative eigensolvers. I here briefly review the eigendecomposition and the chosen eigensolver.

The eigendecomposition

$$\mathbf{T} = \mathbf{Q}\mathbf{\Lambda}\mathbf{Q}^{-1} \tag{1.8}$$

transforms a full rank square matrix $\mathbf{T}$ into diagonal matrix $\mathbf{\Lambda}$ formed by its eigenvalues $\mathrm{diag}(\lambda_0, \lambda_1, ..., \lambda_{N-1})$ and $\mathbf{Q} = (q_0, q_1, ...q_{N-1})$, $\mathbf{Q}^{-1} = (q_0^{-1}; q_1^{-1}; ...q_{N-1}^{-1})$ are matrices formed by the right (column) and left (row) eigenvectors of $\mathbf{T}$. For simplicity we index eigenvalues in descending order of magnitude, $|\lambda_0| \geqslant |\lambda_1| \geqslant ... \geqslant |\lambda_{N-1}|$. Iterative eigenvalue algorithms solve for one or a few eigenvalues and its corresponding eigenvector, usually the leading ones, based on the matrix-vector operation $\mathbf{w} = \mathbf{T}\mathbf{v}$. Since this operation can be conducted without explicitly storing the full matrix $\mathbf{T}$, the space complexity may be controlled within the order of vector size, $\mathcal{O}(N)$. This scheme is extremely useful for the treatment of high-dimensional matrices, for which a direct decomposition (Eq. (1.8)) quickly becomes intractable.

1.3.1 Power iteration

One of the simplest iterative eigenvalue algorithm is the power iteration. Given an initial random vector $\mathbf{v}^{(0)}$ and repeatedly conduct

$$\mathbf{w}^{(\ell+1)} = \mathbf{T}\mathbf{v}^{(\ell)},$$
$$\mathbf{v}^{(\ell+1)} = \mathbf{w}^{(\ell+1)}/\|\mathbf{w}^{(\ell+1)}\|,$$

where $\|\cdot\|$ stands for the Euclidean norm. $\mathbf{v}^{(\ell+1)}$ will converges to the leading eigenvector q_0 with error decays proportional to λ_1/λ_0.

1.3.2 Arnoldi iteration

Similarly, assuming the initial vector is in the null space of q_0, then the power iteration will asymptotically give

$$\mathbf{T}^{\ell}(\mathbf{v}^{(0)} - q_0) \sim q_1,$$

or equivalently, the space spanned by $(\mathbf{T}^{(\ell)}\mathbf{v}^{(0)}, \mathbf{T}^{(\ell+1)}\mathbf{v}^{(0)})$ asymptotically converges to span$[(q_0, q_1)]$ and in general, $(\mathbf{T}\mathbf{v}^{(0)}, \mathbf{T}^2\mathbf{v}^{(0)}, ..., \mathbf{T}^n\mathbf{v}^{(0)})$ is called the Krylov subspace which can be used to approximate first n leading eigenvalues and eigenvectors through the Arnoldi iteration,

Algorithm 1 Arnoldi iteration [35]

```
b_0 ← random unit vector
for i in (1, 2, ..., n) do
    v ← T b_{i-1}
    for j in (1, ..., i) do
        h_ji = b_j^* v
        v ← v − h_ji b_j
    end for
    h_{i+1,i} = ‖v‖
    b_i ← v/h_{i+1,i}
end for
```

where "*" denotes the conjugate transpose. The outer loop performs matrix-vector multiplication and the inner loop orthogonalizes the bases $(b_0, ..., b_n) \equiv \mathbf{B}_n$.

Also, the scalars h_{ji} form a upper Hessenberg matrix $\mathbf{H}_n$ that is decomposed from $\mathbf{T}$,

$$\mathbf{H}_n = \mathbf{Q}^* \mathbf{T} \mathbf{Q} \tag{1.9}$$

and the eigenvalues of the low-dimensional matrix $\mathbf{H}_n$ can be easily calculated through simple algorithms such as aforementioned power iteration or QR iteration. These eigenvalues are called the Ritz values of the original matrix $\mathbf{T}$, and indeed tends to converge to the leading eigenvalues of $\mathbf{T}$.

When $\mathbf{T}$ is a symmetric matrix, the Hessenberg matrix $\mathbf{H}_n$ reduces to a tridiagonal matrix and the Arnoldi iteration is reduced to the Lanczos method.

1.3.3 Implicitly restarted Arnoldi method and ARPACK

A further modification of the Arnoldi method is known as the implicitly restarted Arnoldi method. A high-level description of the algorithm is as follows.

1. Conduct an Arnoldi iteration of step $n_{\text{cv}} > n_{\text{ev}}$, where n_{ev} is the number of eigenvalues required, to construct the Hessenberg matrix and solve for Ritz values.

2. Divide the vectors to a wanted set of length n_{ev} and unwanted set of the remaining, according to the corresponding Ritz values.

3. After shifting vectors in the wanted set against the unwanted set, one conducts the Arnoldi iteration again to extend these n_{ev} vectors into length of n_{cv}, and repeats the process until convergence is met.

This method has since been implemented by ARPACK [4], which is widely used in scientific computation packages such as Mathematica, MATLAB and SciPy [36]. In this thesis, the Spectralib [37]—a C++ open source reimplementation of the ARPACK is used. By default, n_{cv} is set to be $2n_{\text{ev}} + 1$ for $n_{ev} \geqslant 2$ or $n_{\text{cv}} = 5$ if only one eigenvalue is required. The convergence tolerance is set to 10^{-10}.

2

Transfer matrix method

In this chapter I describe the numerical transfer matrix method of the next-nearest-neighbor Ising models.

Because multiple models are considered, let us first define the notation for them. TM prescripts are thus used to distinguish between the ANNNI (A), BNNNI (B), DNNI (D) and 3NNI (3) models as well as to denote the direction of propagation. For the ANNNI model, because the interaction is anisotropic, the TM can be propagated either perpendicularly ($_{\perp,\mathrm{A}}$TM) [18] or parallel ($_{\parallel,\mathrm{A}}$TM) [19] to the direction of the next-nearest-neighbor interaction. Although the former is markedly smaller $2^L \times 2^L$ (vs $4^L \times 4^L$), in the modulated regime the latter converges much faster to the asymptotic scaling as L increases. For the DNNI model, because interactions reach no further than the first subsequent layer, $_{\perp,\mathrm{D}}$TM can be constructed by modifying

This and the next Chapters are adapted from the following publications: (i) Y. Hu, P. Charbonneau, Resolving the two-dimensional axial next-nearest-neighbor Ising model using transfer matrices, Phys. Rev. B 103, 094441 (2021); (ii) Y. Hu, P. Charbonneau, Numerical transfer matrix study of frustrated next-nearest-neighbor Ising models on square lattices, arXiv preprint arXiv:2106.08442 (2021); (iii) Y. Hu, P. Charbonneau, Comments on "Kosterlitz-Thouless-type caging-uncaging transition in a quasi-one-dimensional hard disk system", arXiv:2009.11194 (2020).

$_{\perp,\mathrm{A}}$TM and is thus also of size $2^L \times 2^L$. For the BNNNI and 3NNI models, TM propagation along the diagonal of the square lattice, $_{/}$TM, has been suggested as preferable at finite L [20], in order to better capture the ordering in the direction of the antiphase modulation. This choice also results in a TM of size $2^L \times 2^L$.

In the following, I first introduce the sparse matrix decomposition approach, then the approach of reducing the matrix size. For each approach, I first present in the context of ANNNI model in $d = 2$, then generalized to DNNI, BNNNI and 3NNI models.

2.1 Decomposition for the matrix-vector multiplication

Although transfer matrix entries are straightforwardly expressed (Eq. (1.4)), storing the whole matrix $\mathbf{T}$ in memory becomes quickly beyond practical reach as L increases. The solution relies on using iterative eigenvalue algorithms (such as power iteration or Krylov subspace-based iterations) that only require a matrix-vector multiplication subroutine, with vector $\mathbf{v}$ as input and $\mathbf{w} = \mathbf{T}\mathbf{v}$ as output, and thus avoid explicitly storing $\mathbf{T}$. Because $\mathbf{T}$ is structured, we further decompose it into a product of sparse matrices, which saves additional memory space as well as computer time. In this section, we first introduce the algorithm in the context of ANNNI model in $d = 2$, and then generalize it to the DNNI and 3NNI (include BNNNI) models.

2.1.1 ANNNI model propagated perpendicular to the axial direction

We first consider the $_{\perp}$TM case for the ANNNI model [Fig. 2.1(a)]. In this case, we denote the spin layer state $\mathbf{s} = (\{\pm 1\}^L)$ as an L dimensional binary vector, which is encoded with an L-bit unsigned integer, a, so that $0 \leqslant a \leqslant 2^L - 1$ naturally include all possible layer configurations with $a_1, ..., a_L \in \{0, 1\}$. The physical state $\mathbf{s}$ and machine-expressed state a is related by the simple mapping $a_i = 1 \to s_i = 1$ and $a_i = 0 \to s_i = -1$.

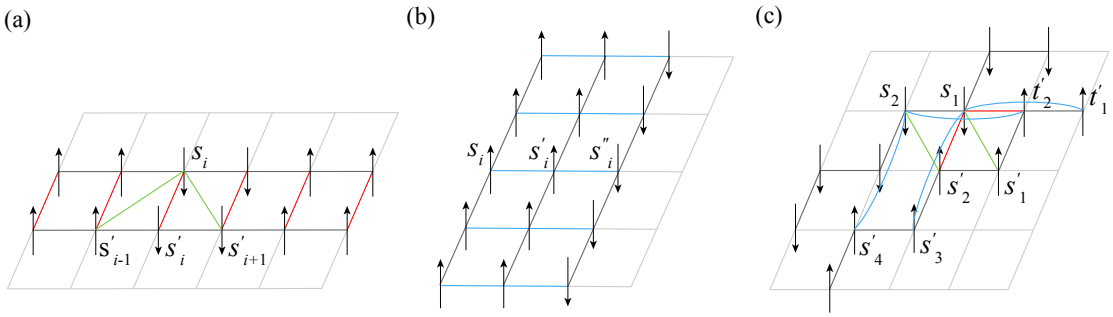

FIGURE 2.1: Schematics of inter-layer interaction in (a) ${}_{\perp,\mathrm{A}}$TM and ${}_{\perp,\mathrm{D}}$TM, (b) ${}_{\parallel,\mathrm{A}}$TM and ${}_{\parallel,3}$TM, (c) ${}_{/,3}$TM. Black lines denote spin layers; red, blue and green lines denote the inter-layer Ising nearest-neighbor interaction, (bi)axial NNN interaction, and diagonal interactions, respectively. Note that for (c) the inter-layer Ising nearest-neighbor interaction for $(\mathbf{s}, \mathbf{s}')$ involves every other spin $s_2, s_4, ...$ on a layer.

The energetic contribution of intra-layer interactions of this state is then

$$V_x(a) = -J \sum_{i=1}^{L} s_i s_{i+1} + \kappa J \sum_{i=1}^{L} s_i s_{i+2} - h \sum_{i=1}^{L} s_i. \tag{2.1}$$

Technically, this expression can be evaluated using bitwise operations. For convenience we first define the net number of positive spins as a function of a, such that $\mathrm{netp}(a) = 2\,\mathrm{popc}(a) - L$, where popc counts the bits set to 1. One can then write

$$V_x(a) = J\,\mathrm{netp}(a \wedge \mathrm{rol}(a,1)) - \kappa J\,\mathrm{netp}(a \wedge \mathrm{rol}(a,2)) - h\,\mathrm{netp}(a), \tag{2.2}$$

where rol is rotate-left-shift (ror is similarly rotate-right-shift) and $\wedge$ is bitwise xor. Similarly, the contribution of the energy of the neighboring layer reads

$$\begin{aligned} V_z(a,a') &= -J \sum_{i=1}^{L} s_i s'_i \\ &= J\,\mathrm{netp}(a \wedge a'). \end{aligned} \tag{2.3}$$

Formally, the transfer matrix $\mathring{\mathbf{T}}$ of size $N_{\mathrm{states}} = 2^L$ (shorthand for ${}_{\perp,\mathrm{A}}\mathring{\mathbf{T}}$) has entries

$$\mathring{\mathbf{T}}_{aa'} = e^{-\beta(V_x(a)+V_z(a,a'))} = \mathbf{T}^x_{a,a} \times \mathbf{T}^z_{a,a'}. \tag{2.4}$$

The binary representation of the entry index a, a' naturally gives the spin configuration of the corresponding layer state, as described above. $\mathring{\mathbf{T}}$ can further be decomposed into a diagonal matrix $\mathbf{T}^x$ with entries $\mathbf{T}^x_{a,a} = e^{-\beta V_x(a)}$ and a symmetric (and centrosymmetric) matrix $\mathbf{T}^z$ with entries $\mathbf{T}^z_{a,a'} = e^{-\beta V_z(a,a')}$.

The partition function of an N-layer system can be expressed using $\mathrm{tr}\left(\mathring{\mathbf{T}}^N\right)$, which however is not symmetric. To leverage the efficiency of fast numerical eigensolvers for symmetric matrices, we define an alternate symmetric transfer matrix

$$\mathbf{T} = (\mathbf{T}^x)^{1/2}\mathbf{T}^z(\mathbf{T}^x)^{1/2}. \tag{2.5}$$

which has the same the eigenvalues as the original matrix, and eigenvectors related by

$$\begin{cases} \varphi(\mathbf{T}) & = (\mathbf{T}^x)^{-1/2}\varphi(\mathring{\mathbf{T}}), \\ \varphi^{-1}(\mathbf{T}) & = \varphi^{-1}(\mathring{\mathbf{T}})(\mathbf{T}^x)^{1/2}, \end{cases} \tag{2.6}$$

where the superscript -1 denotes the left eigenvector. In zero external field, $h = 0$, $\mathbf{T}$ is further centrosymmetric ($\mathbf{T}_{a,a'} = \mathbf{T}_{2^L-a-1,2^L-a'-1}$). As a result of this transformation, we have that: (i) all eigenvalues are real; (ii) all eigenvectors are orthogonal; (iii) every eigenvector is either symmetric or skew-symmetric [38] when $h = 0$.

Because the size of $\mathbf{T}$ grows exponentially with L, storing the full matrix in memory becomes first inefficient and then impractical as L increases. However, a subroutine that computes matrix-vector multiplications on the fly can be used to extract the first several leading eigenvalues and eigenvectors. A direct multiplication requires $\mathcal{O}(4^L)$ arithmetic operations, but can be reduced by factorizing $\mathbf{T}^z$ into sparse matrices as [39]

$$\mathbf{T}^z = \mathbf{T}^{z,L}\mathbf{T}^{z,L-1}\cdots\mathbf{T}^{z,1}, \tag{2.7}$$

where $\mathbf{T}^{z,i}$ has two nonzero entries in each row,

$$\begin{cases} \mathbf{T}^{z,i}_{a,a} = e^{\beta J}, \\ \mathbf{T}^{z,i}_{a,a'} = e^{-\beta J}. \end{cases} \tag{2.8}$$

The off-diagonal indexes $a' = a \wedge \mathrm{rol}(1, i-1)$ here denote the configurations obtained by flipping the i-th spin from a. Note that $\mathbf{T}^{x,i}$ is transformed from $\mathbf{T}^{z,1}$ by re-indexing a to $\mathrm{rol}(a, i-1)$, formulated by the permutation operation

$$\mathbf{T}^{z,i} = (\mathbf{P}^T)^{i-1}\mathbf{T}^{z,1}\mathbf{P}^{i-1} \tag{2.9}$$

where $\mathbf{P}^i$ is the permutation matrix with indexes (a, a') to be 1 and 0 otherwise. Inserting Eq. (2.9) into Eq. (2.7) and knowing $\mathbf{P}^T\mathbf{P} = \mathbf{I}; \mathbf{P}^L = \mathbf{I}$ gives

$$\mathbf{T}^z = (\mathbf{P}\mathbf{T}^{z,1})^L. \tag{2.10}$$

In summary, the matrix-vector multiplication can be conducted by a sequence of multiplication with sparse matrices

$$\mathbf{T}\mathbf{v} = (\mathbf{T}^x)^{1/2}(\mathbf{P}\mathbf{T}^{z,1})^L(\mathbf{T}^x)^{1/2}\mathbf{v} \tag{2.11}$$

with complexity $\mathcal{O}(2^L L)$.

In addition, we have $\mathbf{T}$ is invariant under the permutation of circularly shifting one spin, such that

$$\mathbf{T} = \mathbf{P}^T\mathbf{T}\mathbf{P}, \tag{2.12}$$

where $\mathbf{P}^L = \mathbf{I}$. If φ is an eigenvector of $\mathbf{T}$, then $\mathbf{P}\varphi$ is also an eigenvector of $\mathbf{T}$ associated with same eigenvalue λ, because

$$\mathbf{T}(\mathbf{P}\varphi) = \mathbf{P}\mathbf{T}\varphi = \lambda\mathbf{P}\varphi. \tag{2.13}$$

As a result, an eigenvector of non-degenerate eigenvalue is invariant under the permutation of $\mathbf{P}$, and degenerate eigenvectors associated with degenerate eigenvalue (and their linear combinations) form a cyclic group. This structural property can be used to optimize the extraction of leading eigenvalues, as we will describe in Sec. 2.2.

2.1.2 *ANNNI model propagated along the axial direction*

We now consider $_{\parallel}$TM for the ANNNI model [Fig. 2.1(b)]. In this case, we denote three subsequent layers as a, a', a'' where the state of each layer is encoded as an L-bit integer, as above. The energetic contribution of a then includes NN interactions with itself and with a' as well as NNN interaction with a'',

$$\begin{cases} V_x(a,a') & = -J\sum_{i=1}^{L} s_i s_{i+1} - J\sum_{i=1}^{L} s_i s_i' \\ & \quad -h\sum_{i=1}^{L} s_i, \\ V_z(a,a'') & = \kappa J \sum_{i=1}^{L} s_i s_i''. \end{cases} \tag{2.14}$$

The bitwise operations then reads

$$\begin{cases} V_x(a,a') & = J\,\mathrm{netp}(a \wedge \mathrm{rol}(a,1)) + J\,\mathrm{netp}(a \wedge a') \\ & \quad -h\,\mathrm{netp}(a), \\ V_z(a,a') & = -\kappa J\,\mathrm{netp}(a \wedge a''). \end{cases} \tag{2.15}$$

We then define the transfer matrix $\mathbf{T}$ (shorthand for $_{\parallel,\mathrm{A}}\mathbf{T}$) with entries

$$\begin{aligned} \mathbf{T}_{(a,a'),(a',a'')} &= e^{-\beta(V_x(a,a')+V_z(a,a''))} \\ &= \mathbf{T}^x_{(a,a'),(a,a')} \cdot \mathbf{T}^z_{(a,a'),(a',a'')}, \end{aligned} \tag{2.16}$$

The row and column of $\mathbf{T}$ are indexed by a combination of two L-bit integers (a, a') and (a', a''), so that $N_{\mathrm{states}} = 2^{2L}$. This construction results in a matrix of size $4^L \times 4^L$. Again we decompose $\mathbf{T}$ into a diagonal matrix $\mathbf{T}^x$ with entries $\mathbf{T}^x_{(a,a'),(a,a')} = e^{-\beta V_x(a,a')}$ and a sparse matrix $\mathbf{T}^z$ with entries $\mathbf{T}^z_{(a,a'),(a',a'')} = e^{-\beta V_z(a,a'')}$ and 0 otherwise. The number of nonzero entries is then 8^L. The partition function of N-layer system is given by $\mathrm{tr}\left(\mathbf{T}^N\right)$. In contrast to Section 2.1.1, $\mathbf{T}^z$ is no longer symmetric. A generic eigensolver is then required to solve the eigenproblem. Although generic eigenvalues can take complex values, the leading eigenvalue is always a positive real number as are the entries of the leading (left and right) eigenvectors, from the Perron-Frobenius theorem.

Because the value of the nonzero entries in $\mathbf{T}^z$ does not depend on a', ${}_{\parallel,\mathrm{A}}\mathbf{T}^z_{(a,a'),(a',a'')}$ can be mapped into ${}_{\perp,\mathrm{A}}\mathbf{T}^z_{a,a''}$ with the interaction strength replaced by κJ (instead of $-J$ in Eq. (2.8)). Given that the complexity for the matrix-multiplication with ${}_{\perp,\mathrm{A}}\mathbf{T}^z$ is $\mathcal{O}(2^L L)$, and that there are 2^L operations (for different a') in total, the complexity for the matrix-multiplication with ${}_{\parallel,\mathrm{A}}\mathbf{T}^z$ is $\mathcal{O}(4^L L)$. Hence, the matrix-multiplication operation on ${}_{\parallel,\mathrm{A}}\mathbf{T}$ also has a time complexity of $\mathcal{O}(4^L L)$.

2.1.3 DNNI Model

Because the horizontal and vertical directions of the DNNI model are equivalent, a single transfer matrix can be defined. The contribution of intra-layer states,

$$V_x(a) = -J\sum_{i=1}^{L} s_i s_{i+1} - h\sum_{i=1}^{L} s_i, \tag{2.17}$$

is independent of κ, while the energetic contribution of neighboring layers reads

$$V_z(a,a') = -J\sum_{i=1}^{L} s_i s'_i + \kappa J\left(\sum_{i=1}^{L} s_i s'_{i-1} + \sum_{i=1}^{L} s_i s'_{i+1}\right). \tag{2.18}$$

The transfer matrix $\mathbf{T}$ (shorthand for ${}_{\perp,\mathrm{D}}\mathbf{T}$) can thus be decomposed into intra-layer and inter-layer interactions as in Eq. (2.5). For the DNNI model, the inter-layer matrix $\mathbf{T}^z$ is also symmetric (and centrosymmetric when $h = 0$) with entries $\mathbf{T}^z_{a,a'} = e^{-\beta V_z(a,a')}$.

Again, $\mathbf{T}^z$ can be decomposed to reduce the complexity of the matrix-vector multiplication, but we can no longer use Eq. (2.10). This scheme drops information about s'_{i-1} after computing the inter-layer interaction for s_{i-1}, which, although fine for the ANNNI model, for the DNNI model leaves out the interaction between s_i and its diagonal neighbors, s'_{i-1} and s'_{i+1} [Fig. 2.1(a)]. To make up for this loss of information, we introduce an auxiliary spin $t_1 = s'_i$ for spin indexes $i = 1...L$ during the propagation. Because periodic boundary conditions require $s_1 = s_{L+1}$, we

introduce an additional auxiliary spin for $r_1 = s'_1$. (For the ANNNI model, s_L does not interact with s'_1.) The factorization of $\mathbf{T}^z$ is thus

$$\begin{aligned} \mathbf{T}^z &= \mathbf{S}^{-1}\mathbf{T}^{z,L}\mathbf{T}^{z,L-1}...\mathbf{T}^{z,1}\mathbf{S} \\ &= \mathbf{S}^{-1}(\mathbf{P}\mathbf{T}^{z,1|r_1})(\mathbf{P}\mathbf{T}^{z,1})^{L-1}\mathbf{S}. \end{aligned} \tag{2.19}$$

The auxiliary matrix $\mathbf{S}$ (and $\mathbf{S}^{-1}$) maps (recovers) a vector of dimension 2^L to (from) 2^{L+2}, namely,

$$(\mathbf{S}x)(\{s_1, s_2, ..., s_L, ..., t_1, r_1\}) = \begin{cases} x(s_1, ..., s_L), & t_1 = s_L \text{ and } r_1 = s_1 \\ 0, & \text{otherwise,} \end{cases} \tag{2.20}$$

and

$$(\mathbf{S}^{-1}y)(a) = \sum_{t_1, r_1} y(a, t_1, r_1). \tag{2.21}$$

The matrix $\mathbf{T}^{z,1}$, which denotes the contribution on the inter-layer interaction for one spin, s_1, has entries

$$\mathbf{T}^{z,1}(\{s_1, s_2, ..., s_L, t_1, r_1\}, \{s'_1, s'_2, ..., s'_L, t'_1, r'_1\}) =$$

$$\begin{cases} e^{\beta J s_1 s'_1 - \kappa\beta J s_1(t'_1 + s'_2)}, & s_i = s'_i (i = 2...L), \\ & t_1 = s'_1, r_1 = r'_1, \\ 0, & \text{otherwise.} \end{cases} \tag{2.22}$$

The permutation matrix $\mathbf{P}$ shifts spins $\{s_1, ..., s_L\}$ to $\{s_2, ..., s_L, s_1\}$ but does not change auxiliary spins. Note that the term $\mathbf{T}^{z,1|r_1}$ in Eq. (2.19) reflects the periodic boundary condition that replaces s'_2 by r_1.

The overall time complexity of matrix-vector multiplication remains $\mathcal{O}(2^L L)$. The size of the temporary vector is quadrupled compared to ${}_\perp$TM for the ANNNI model because two auxiliary spins had to be included, but can be halved by tracing r_1 in the code (instead of as a vector index) because it is only invoked for operations on $\mathbf{T}^{z,L}$.

2.1.4 BNNNI Model and 3NNI model

Because the BNNNI model can be considered as a special case of the 3NNI model with $\kappa' = 0$, we only need to consider the later. One possible transfer matrix construction thus requires but minimal modification from ${}_{\parallel,\mathrm{A}}\mathrm{TM}$, namely including diagonal nearest-neighbor and axial next-nearest-neighbor interactions in the intra-layer part $\mathbf{T}_{(a,a'),(a,a')}$,

$$ {}_{\parallel,3}\mathbf{T}^{x}_{(a,a'),(a,a')} = \exp\{-\beta[V_x(a,a') + V_{x,\mathrm{B}}(a) + V_{x,\mathrm{D}}(a,a')]\} \tag{2.23} $$

where $V_{x,\mathrm{B}}$ and $V_{x,\mathrm{D}}$ are missing from the ANNNI model in Eq. (2.15),

$$ \begin{aligned} V_{x,\mathrm{B}}(a) &= -\kappa J \,\mathrm{netp}(a \wedge \mathrm{rol}(a,2)), \\ V_{x,\mathrm{D}}(a,a') &= -\kappa' J[\mathrm{netp}(a \wedge \mathrm{rol}(a',1)) + \mathrm{netp}(a \wedge \mathrm{ror}(a',1))]. \end{aligned} \tag{2.24} $$

The structure and complexity of the remaining algorithm then remain unchanged.

However, as stated in Sec. 3.3, the checkerboard and diagonal striped phases of the BNNNI and 3NNI models are naturally modulated along the diagonals of a square lattice. To study the correlation length of these modulations and to minimize the finite-size disturbances observed in ${}_{\parallel,3}\mathbf{T}$, we thus consider a transfer matrix propagated along the diagonal direction, ${}_{/,3}\mathbf{T}$, hence generalizing the approach of Ref. [20]. Note that this arrangement requires L to be even.

As in Eq. (2.5), the resulting transfer matrix can be decomposed into intra-layer and inter-layer contributions. The intra-layer matrix can be computed directly, and the inter-layer matrix $\mathbf{T}^z$ can be decomposed similarly as for the DNNI model (Eq. (2.19))

$$ \mathbf{T}^z = \mathbf{S}^{-1}\mathbf{T}^{z,L}\mathbf{T}^{z,L-1}...\mathbf{T}^{z,2}\mathbf{S} = \mathbf{S}^{-1}(\mathbf{P}\mathbf{T}^{z,2|t_1,t_2})(\mathbf{P}\mathbf{T}^{z,2})^{L/2-1}\mathbf{S}. \tag{2.25} $$

The auxiliary matrix $\mathbf{S}$ (and $\mathbf{S}^{-1}$) then maps (recovers) a vector of dimension 2^L to

(from) 2^{L+4},

$$(\mathbf{S}x)(\{s_1, s_2, ..., s_L, ..., t_1, t_2, r_1, r_2\}) =$$

$$\begin{cases} x(s_1, ..., s_L), & (t_1, t_2, r_1, r_2) = (s_{L-1}, s_L, s_1, s_2) \\ 0, & \text{otherwise,} \end{cases} \tag{2.26}$$

and

$$(\mathbf{S}^{-1}y)(a) = \sum_{t_1,t_2,r_1,r_2} y(a, t_1, t_2, r_1, r_2). \tag{2.27}$$

The matrix $\mathbf{T}^{z,2}$, which denotes the contribution on the inter-layer interaction for two spins, s_1 and s_2, [Fig. 2.1(c)], has entries

$$\mathbf{T}^{z,2}(\{s_1, ..., s_L, t_1, t_2, r_1, r_2\}, \{s'_1, ..., s'_L, t'_1, t'_2, r'_1, r'_2\}) =$$

$$\begin{cases} \exp\{-\beta J[(s'_1(t_2 + s_2) & s_i = s'_i (i = 3...L), \\ -\kappa(s'_1(t_1 + s_3) + s'_2(t_2 + s_4)) & (t_1, t_2, r_1, r_2) \\ -\kappa'(s'_1 s_1 + s'_2 s_2)] & = (s'_1, s'_2, r'_1, r'_2), \\ \\ 0, & \text{otherwise.} \end{cases} \tag{2.28}$$

The permutation matrix $\mathbf{P}$ shifts layer configurations by two spins, i.e., $\{s_1, s_2, ..., s_L\} \rightarrow \{s_3, ..., s_L, s_1, s_2\}$. The term $\mathbf{T}^{z,2|r_1,r_2}$ in Eq. (2.25) reflects the periodic boundary condition that replaces s'_3, s'_4 by r_1, r_2.

This arrangement of auxiliary spins can be viewed as a generalization of the approach used for the DNNI model. A spin s_i here involves interactions with $s_{i\pm2}$, thus going beyond $s_{i\pm1}$ for the DNNI model. In general, for models with inter-layer interactions between s_i and $s'_{i\pm b}$, $2b$ auxiliary spins are needed, among which t spins are associated with an extended vector, then of size 2^{L+b}. The size of this vector controls the space complexity for the matrix-vector multiplication. In addition to the 2^b loops for different choices of r spins, the time complexity is then $\mathcal{O}(2^{L+2b}L)$. For ${}_{/,3}\mathbf{T}$, in particular, the number of operations and the intermediate vector size are $2^4 = 16$ and $2^2 = 4$ times that for ${}_{\perp,\mathrm{A}}\mathrm{TM}$, respectively.

2.2 Reducing space complexity with symmetry

In this section we describe computational schemes used to reduce the size of the transfer matrix, and thus significantly decrease the algorithmic space complexity. The key idea is to identify equivalent states in order to construct orthogonal bases (or irreducible representations [18], as have been implemented in related models [21, 39]). We here adapt this method following the framework of the structured matrix decomposition described in the previous section. We first derive the general method for structured matrices with certain permutation invariance, and then analyze the complexity of the transfer matrix involved in solving the models of interest.

2.2.1 General case

Denote $\mathbf{T}$ as an $n \times n$ matrix that is invariant under permutations $\mathbf{P}_1$, $\mathbf{P}_2$, ..., $\mathbf{P}_g$, such that $\mathbf{P}_i^T \mathbf{T} \mathbf{P}_i = \mathbf{T}$ for $i = 1, ..., g$ and that these transformations form a symmetry group $\mathcal{G}$. Matrix indexes are then grouped by these transformations. For example, for a centrosymmetric matrix, under the transformation of $\mathbf{P}^T\mathbf{T}\mathbf{P}$ where $\mathbf{P} = (e_n, e_{n-1}, ..., e_1)$, row and column indexes are permuted as $0 \to n-1$, $1 \to n-2$ and so on. The indexes i and $n-i-1$ are then deemed equivalent. There are $n/2$ equivalent sets in total.

We next construct a (non-square) matrix with orthogonal columns

$$\mathbf{Q} \equiv \begin{bmatrix} 1/\sqrt{g_1} & 0 & ... & ... & 0 \\ 0 & ... & 1/\sqrt{g_i} & ... & ... \\ ... & ... & ... & ... & 1/\sqrt{g_n} \\ 1/\sqrt{g_1} & ... & ... & ... & ... \end{bmatrix} \tag{2.29}$$

of size $n \times m$, where m is the number of sets of equivalent indexes (not to be confused with the magnetization). Each column in $\mathbf{Q}$ is a column vector corresponding to an equivalent index set of size g_i. The entries in $\mathbf{Q}_i$ are nonzero, and set to $1/\sqrt{g_i}$, if and only if its row index is in the set. Applying the similarity transformation on $\mathbf{T}$

with these bases, we obtain a matrix of size $m \times m$

$$\mathbf{M} = \mathbf{Q}^T \mathbf{T} \mathbf{Q}. \tag{2.30}$$

We then establish the following claim:

Theorem 1. *If* $\mathbf{T}$ *is primitive (in the context of Perron-Frobenius theorem),* $\mathbf{M}$ *and* $\mathbf{T}$ *have the same leading eigenvalue with eigenvector* $\varphi_1(\mathbf{T}) = \mathbf{Q}\psi_1(\mathbf{M})$.

In this way, we can compute the partition function by considering the compressed transfer matrix $\mathbf{M}$. The proof is obtained as follows.

Lemma 1. *The eigenvalues of* $\mathbf{M}$ *are also eigenvalues of* $\mathbf{T}$.

Proof. First, we observe that $\mathbf{Q}^T\mathbf{Q} = \mathbf{I}$. Therefore, $\mathbf{Q}$ forms a set of orthogonal basis in a m-dimensional subspace of $\mathbb{R}^n$. Constructing a full rank matrix

$$\hat{\mathbf{Q}} = \begin{pmatrix} \mathbf{Q} & \tilde{\mathbf{Q}} \end{pmatrix} \tag{2.31}$$

where $\tilde{\mathbf{Q}}$ is formed by $(n - m)$ orthogonal basis in the null space of $\mathbf{Q}$. Hence $\hat{\mathbf{Q}}^T\hat{\mathbf{Q}} = \mathbf{I}$. Under the transformation on $\hat{\mathbf{Q}}$,

$$\hat{\mathbf{Q}}^T \mathbf{T} \hat{\mathbf{Q}} = \begin{pmatrix} \mathbf{Q}^T\mathbf{T}\mathbf{Q} & \mathbf{Q}^T\mathbf{T}\tilde{\mathbf{Q}} \\ \tilde{\mathbf{Q}}^T\mathbf{T}\mathbf{Q} & \tilde{\mathbf{Q}}^T\mathbf{T}\tilde{\mathbf{Q}}. \end{pmatrix}$$

Because $\mathbf{TQ} = \mathbf{P}^T\mathbf{TPQ} = \mathbf{P}^T\mathbf{TQ}$ for $\mathbf{P} \in \mathcal{G}$, the rows of the matrix $(\mathbf{TQ})$ are invariant under permutation of $\mathbf{P}^T$ (and so does $\mathbf{P}$). In other words, rows related by all $\mathbf{P} \in \mathcal{G}$ in $(\mathbf{TQ})$ are identical. Hence one can construct a matrix $\mathbf{A}$ of size $m \times m$ and let

$$\mathbf{TQ} = \mathbf{QA}.$$

Notice that

$$\mathbf{Q}^T\mathbf{TQ} = \mathbf{Q}^T\mathbf{QA} = \mathbf{A},$$

hence $\mathbf{A} = \mathbf{M}$. Note this step is necessary because one cannot directly obtain the identity $\mathbf{TQ} = \mathbf{QM}$ by multiplying $\mathbf{Q}$ on the left in both sides of Eq. (2.30), given that $\mathbf{QQ}^T \neq \mathbf{I}$.

We then have

$$\hat{\mathbf{Q}}^T\mathbf{T}\hat{\mathbf{Q}} = \begin{pmatrix} \mathbf{M} & \mathbf{Q}^T\mathbf{T}\tilde{\mathbf{Q}} \\ \tilde{\mathbf{Q}}^T\mathbf{QM} & \tilde{\mathbf{Q}}^T\mathbf{T}\tilde{\mathbf{Q}}. \end{pmatrix} = \begin{pmatrix} \mathbf{M} & \mathbf{Q}^T\mathbf{T}\tilde{\mathbf{Q}} \\ 0 & \tilde{\mathbf{Q}}^T\mathbf{T}\tilde{\mathbf{Q}}. \end{pmatrix}$$

is a block triangular matrix. Hence $\lambda(\mathbf{T})$ is the union of $\lambda(\mathbf{M})$ and $\lambda(\tilde{\mathbf{Q}}^T\mathbf{T}\tilde{\mathbf{Q}})$. □

Lemma 2. *Eigenvectors of non-degenerate eigenvalues in* $\mathbf{T}$ *are also eigenvectors of* $\mathbf{P}$*, namely,* $\mathbf{P}\varphi = a\varphi$ *with* $|a| = 1$*.*

Proof.

$$\mathbf{P}\varphi = \mathbf{P}^T\mathbf{T}\mathbf{P}\varphi = \lambda\varphi$$
$$\Leftrightarrow \mathbf{T}(\mathbf{P}\varphi) = \lambda(\mathbf{P}\varphi),$$

so that $\mathbf{P}\varphi$ is also an eigenvector of λ. Because λ is degenerate, one has $\mathbf{P}\varphi = a\varphi$ with some scalar a. Note that this expression coincides with the eigen-equation of $\mathbf{P}$, so that φ is also an eigenvector of $\mathbf{P}$. Moreover, the eigenvalue of permutation matrix has unit magnitude, i.e., $|a| = 1$. □

Having Lemma 1 and 2, we can now prove the Theorem 1.

Proof. Because $\mathbf{T}$ is primitive, its leading eigenvalue is degenerate and the entries of the leading eigenvectors are all positive. According to Lemma 2, $\mathbf{P}\varphi_1 = \varphi_1$. In other words, entries of the equivalent indices in φ_1 are of the same value. Arranging the entries of equivalent indices as an m-dimensional vector ψ such that $\varphi_1 = \mathbf{Q}\psi$ and

thus $\mathbf{Q}^T\varphi_1 = \psi$, one gets

$$\begin{aligned}
\mathbf{T}\varphi_1 &= \mathbf{TQ}\psi \\
\mathbf{Q}^T\mathbf{T}\varphi_1 &= \mathbf{Q}^T\mathbf{TQ}\psi \\
\lambda_1\mathbf{Q}^T\varphi_1 &= \mathbf{M}\psi \\
\lambda_1\psi &= \mathbf{M}\psi,
\end{aligned}$$

Hence $\mathbf{M}$ also has eigenvalue λ_1, which is associated with eigenvector ψ. Because the eigenvalues of $\mathbf{M}$ is a subset of eigenvalues of $\mathbf{T}$ (Lemma 1), λ_1 is also the leading eigenvalue of $\mathbf{M}$ and non-degenerate. □

Two-dimensional spin models under periodic boundary condition are invariant under rotation of one spin (a C_n axis) as well as under counting spins backwards (a σ_v reflection), and hence belongs to the C_{nv} point group. In absence of external field, $h = 0$, the model is also invariant under flipping all spins (a σ_h reflection), and hence it belongs to the D_{nh} group. The dimension of $\mathbf{M}$ is asymptotically reduced by a factor which equals the order of the symmetry group—$2L$ for C_{nv} and $4L$ for D_{nh} (Fig. 2.2). In this way, the transfer matrix size can be compressed by a factor of $2L$ (or $4L$ if $h = 0$ and only the leading eigenvalue is needed).

2.2.2 $_\perp$TM *and* $_/$TM

We now adapt this compressed matrix to our transfer matrix calculation. We first consider $_\perp$TM (the construction of $_/$TM is very similar to $_\perp$TM, as we will see later). Directly implementing Eq. (2.11) to calculate the matrix-vector multiplication

$$\begin{aligned}
\mathbf{w} = \mathbf{Mv} &= \mathbf{Q}^T\mathbf{TQv} = \mathbf{Q}^T(\mathbf{T}^x)^{1/2}(\mathbf{PT}^{z,1})^L(\mathbf{T}^x)^{1/2}\mathbf{Qv} \\
&= \mathbf{Q}^T\mathbf{w}'
\end{aligned} \tag{2.32}$$

gives essentially the same time and space complexity as for conducting $\mathbf{Tv}$.

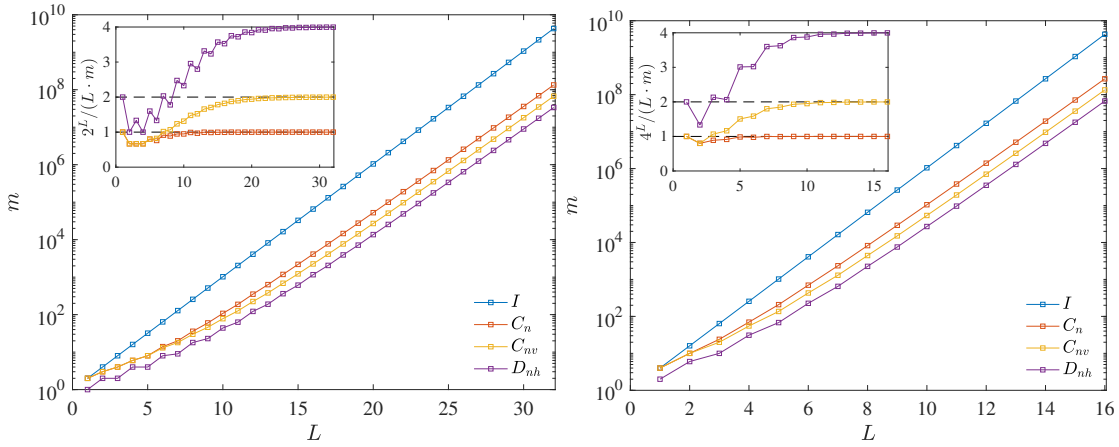

FIGURE 2.2: Number of equivalent state sets (m) of different symmetry group grows with layer length (L) in (left) $_\perp$TM and (right) $_\parallel$TM. Values are obtained in accordance with certain integer series[1]. (insets) m asymptotically scales with N_{states}/L, $N_{\text{states}}/(2L)$ and $N_{\text{states}}/(4L)$ under C_n, C_{nv} and D_{nh} symmetry, respectively.

Further optimization is, however, possible. Observing that entries in the intermediate vector ($\mathbf{w}'_a$) belonging to the same equivalent states ($a \in b$) are identical, we only need to compute one (among g_b identical entries) for each set of equivalent states in $\mathbf{w}'$ to construct $\mathbf{w}$, such that

$$\mathbf{w}_b = \sqrt{g_b}\mathbf{w}'_a. \tag{2.33}$$

To take advantage of this property, we initialize an array of equivalent states, denoted $[b]$, containing one of the states (a) in the set as well as the set size (g_b). The number of equivalent sets approaches $2^L/(4L)$ for $h = 0$ and $2^L/(2L)$ otherwise. In both cases $[b]$ has a space complexity of $\mathcal{O}(2^L/L)$. This list can be constructed in two ways with offer different balances in space/time complexity. The first is to set up a temporary array of 2^L bits (thus with a $\mathcal{O}(2^L)$ space complexity) and scanning once (thus with a $\mathcal{O}(2^L)$ time complexity). The second is to enumerate each of the 2^L states and check all of its equivalent states by bit-wise operations (in a $\mathcal{O}(2^L L)$ time complexity), and

[1] For $_\perp$TM: Number of equivalent states under C_n, C_{nv} and D_{nh} symmeytries correspond to OEIS series (`https://oeis.org`) A000031, A000029 and A000011; for $_\parallel$TM: C_n, C_{nv} and D_{nh} equivalent states correspond to OEIS series A001868, A081720 (4th column) and A283846.

push the state to the array only if it has smallest index of all equivalent states. The total number of equivalent state $[\mathcal{O}(2^L/L)]$ then gives the space complexity.

Equation (2.32) can then be evaluated in two parts. First, we compute the inter-layer interactions of all states a with L' leftmost spins having the same configuration, a^ℓ. Denoting the remaining $L - L'$ bits to their right as a^r, we hence have $a \equiv a^\ell.a^r$ where "." is a bit concatenation operation. In practice, we set up an intermediate vector ${}^{a^\ell}\mathbf{v}$ of size $2^{L-L'}$ such that

$$\Big({}^{(0}\mathbf{v})^T, ({}^1\mathbf{v})^T, ..., ({}^{2^{L'}-1}\mathbf{v})^T\Big)^T = \mathbf{Q}\mathbf{v}. \tag{2.34}$$

Decoding each ${}^{a^\ell}\mathbf{v}$ from $[b]$ and $\mathbf{v}$ costs a time $\mathcal{O}(L \times m) = O(2^L)$ and it is run $2^{L'}$ times. For each ${}^{a^\ell}\mathbf{v}$, we further compute

$${}^{a^\ell}\mathbf{w}'' = {}^{a^\ell}\Big((\mathbf{P}\mathbf{T}^{z,1})^{L-L'}(\mathbf{T}^x)^{1/2})\Big) \cdot {}^{a^\ell}\mathbf{v}. \tag{2.35}$$

The time complexity of this step is $\mathcal{O}((L - L')2^{L-L'})$ and it is run $2^{L'}$ times (or $2^{L'-1}$ times for $h = 0$, because $\mathbf{T}$ is then centrosymmetric). Second, for every non-equivalent entry in $\mathbf{w}'$, we also decompose the index $a' = (a'^\ell.a'^r)$ and increment $\mathbf{w}'_{a'}$ by $\exp\big(-\beta V_z(a^\ell, a'^\ell)\big) \cdot {}^{a^\ell}\mathbf{w}''_{a'^r}$. In summary this approach gives

$$\mathbf{w}'_{a'} = (\mathbf{T}^x_{a',a'})^{1/2} \sum_{a^\ell} \exp\big(-\beta V_z(a^\ell, a'^\ell)\big) \cdot {}^{a^\ell}\mathbf{w}''_{a'^r}, \tag{2.36}$$

and the time complexity for this step is $\mathcal{O}(2^{L'} \times m) = O(2^{L'+L}/L)$. Comparing the time complexities of Eq. (2.34), (2.35) and (2.36), we choose $L' = 1 + \lfloor \log_2 L \rfloor$ so that the total time complexity for matrix-vector multiplication remains $\mathcal{O}(2^L L)$ and the space complexity is reduced to $\mathcal{O}(2^L/L)$.

The permutation operations that generate equivalent states for ${}_/$TM slightly differs from ${}_\perp$TM because now the layer has a zigzag shape. Specifically, the system is

invariant after shifting two (instead of one) spins as well as by first shifting one spin and then counting backwards (instead of simply counting backwards). The number of equivalent states m then asymptotically approaches $2^L/L$ (or $2^L/(2L)$ for $h = 0$). Because we consider two spins (s_1, s_2) in every operation in $\mathbf{T}^{z,2}$, we choose (an even) $L' = 2(1 + \lfloor \log_2 L/2 \rfloor)$. The time and space complexities remain the same with $_\perp$TM, but with a larger prefactor.

2.2.3 $_\parallel$TM

Similarly to Eq. (2.32), for $_\parallel$TM the matrix-vector multiplication is decomposed as

$$\mathbf{w} = \mathbf{M}\mathbf{v} = \mathbf{Q}^T\mathbf{T}\mathbf{Q}\mathbf{v} = \mathbf{Q}^T(\mathbf{T}^x)(\mathbf{P}\mathbf{T}^{z,1})^L\mathbf{Q}\mathbf{v} = \mathbf{Q}^T\mathbf{w}'. \tag{2.37}$$

Now, however, $\mathbf{M}$ is not symmetric. In addition to permutation invariance, we can also take advantage of the sparsity of $_\parallel$TM (Sec. 2.1.2) to compute $\mathbf{M} \cdot \mathbf{v}$. The extra space needed is a vector of size 2^L which is much smaller than the vector size of $m = O(4^L/L)$. The time complexity can also be reduced because $\mathbf{w}'$ has identical entries for equivalent states.

The algorithm is as follows. First, we initialize the array of equivalent states $[b]$, as we did for $_\perp$TM, such that each element is a pair of L-bit integers (a, a') that represents this set. Two extra arrays are stored for later bookkeeping purposes:

1. An array of equivalent states for a alone, denoted $[c]$, along with the period of a under cyclic shift. The size of $[c]$ approaches $m' \approx 2^L/(4L)$ for D_{nh} and $m' \approx 2^L/(2L)$ for C_{nv} bases.

2. An array of indexes $[b']$ for each representing state (a, a') in $[b]$ that records the references in $[b]$ corresponding to the equivalent state with layers swapped, (a', a), denoted $b'(a', a)$.

The construction of $[b']$ can follow the construction of $[b]$. For each (a, a') newly appended to $[b]$, we find $b'(a', a)$. If $b'(a', a) \leqslant (a, a')$, a binary search finds the index

of $b'(a', a)$ in $[b]$. (Each binary search takes on average $\mathcal{O}(\log m) = \mathcal{O}(L)$ operations, and hence the overall algorithmic complexity remains unchanged.) In summary, the initialization takes $\mathcal{O}(4^L)$ operations, and storing $[b]$ takes space $\mathcal{O}(4^L/L)$.

Second, we setup the subroutine for the matrix-vector multiplication of Eq. (2.32). Again we denote the indexes of $\mathbf{w}$ and $\mathbf{v}$ as (a, a') and (a', a''), respectively. For each a' in $[c]$, we construct an intermediate vector ${}^{a'}\mathbf{v}$ such that

$$\left(({}^{a'_1}\mathbf{v})^T, ({}^{a'_2}\mathbf{v})^T, ..., ({}^{a'_{m'}}\mathbf{v})^T \right)^T = \mathbf{Q}\mathbf{v}. \tag{2.38}$$

Because each ${}^{a'}\mathbf{v}$ is of size 2^L and m' of these vectors in total, the complexity of this step is $\mathcal{O}(2^L m') = O(4^L/L)$.

For each ${}^{a'}\mathbf{v}$, we compute

$${}^{a'}\mathbf{w}'' = \left(\mathbf{P} \cdot {}_{\perp}\mathbf{T}^{z,1} \right)^L \cdot {}^{a'}\mathbf{v}, \tag{2.39}$$

with $J' = -\kappa J$ in $\mathbf{T}^{z,1}$. It takes $\mathcal{O}(2^L L)$ operations per a', and hence the total complexity of this step is $\mathcal{O}(2^L L \times 2^L/L) = \mathcal{O}(4^L)$.

The entries in the resulting vector, ${}^{a'}\mathbf{w}''_a$ corresponds to those of the intermediate vector $\mathbf{w}'$ with

$$\mathbf{w}'_{b'(a,a')} = \mathbf{T}^x_{b'(a,a'),b'(a,a')} \, {}^{a'}\mathbf{w}''_a. \tag{2.40}$$

Again, we have

$$\mathbf{w}_b = \sqrt{g_b}\mathbf{w}'_a, \tag{2.41}$$

and hence Eq. (2.40) needs to be evaluated $m = O(4^L/L)$ times.

In summary, the time complexity is of $\mathcal{O}(4^L)$, an improvement by a factor of L over that in Sec. 2.1.2. The extra space needed is $\mathcal{O}(m')$ which is marginal given that input and output vectors have sizes $\mathcal{O}(m)$.

2.2.4 Remarks

Thanks to these compressed TMs, evaluation of systems with L up to 36 for ${}_{\perp}$TM, 32 for ${}_{/}$TM and 16 for ${}_{\parallel}$TM is accessible within 60 GB memory. Interestingly, when evaluating $\mathbf{T}$ with an iterative eigensolver, convergence slows down markedly around transition temperatures. In ${}_{\perp}$TM for the ANNNI model with $L = 20$, for example, the slowdown at T_{c} can be as much as $15\times$ that of a typical run away from that temperature. The slowdown for the compressed TM, however, is less pronounced, which facilitates free energy calculations. The compressed TM is therefore better conditioned, which adds extra advantage to this consideration. As a result, the algorithm is numerical stable and generates results with high accuracy. This property is indeed related to the underlying physics. The condition number is defined as the error of the output given an erroneous (or finite precision) input. The specific heat also corresponds to the fluctuation on energy, $\langle(\delta u)^2\rangle = k_B T c$, which means when c is high, the output of the eigenvectors (density of configurations) is very unstable, and leads to a large condition number. The phase transition in physics and convergence theory in computer science are intrinsically related.

A challenge for this decomposition, however, is that subleading eigenvalues of $\mathbf{T}$ can lie either in span($\mathbf{M}$) or in null($\mathbf{M}$). In other words, the spectral gap, which gives the leading correlation length, of $\mathbf{M}$ does not necessarily coincide with that of $\mathbf{T}$. In practice, it is observed that for ${}_{\parallel,\mathrm{A}}\mathbf{T}$, ${}_{\perp,\mathrm{D}}\mathbf{T}$, ${}_{\parallel,3}\mathbf{T}$ and ${}_{/,3}\mathbf{T}$ in $h = 0$, the subleading eigenvectors are all skew-symmetric, and preserved in the compressed TMs with C_{nv} bases. We therefore identify the correlation length from the compressed matrix. For ${}_{\perp,\mathrm{A}}\mathbf{T}$, however, the subleading eigenvalue is doubly degenerate (as in Ref. [18]), and is observed in the null space of $\mathbf{M}$ obtained from C_{nv} bases. The original transfer matrix is thus used to identify the correlation length. As noted in Ref. [18] this is a result of symmetry of the bases. For other models a similar argument might also be

possible.

2.3 Planting configurations via transfer matrices

In this section, I introduce a planting algorithm which generates equilibrium configurations from the leading eigenpairs obtained from the TM approach.

Because the planting scheme proposed is generic and could be applied to any system solvable by transfer matrices, we first describe it in general terms, and then apply it to the next-nearest-neighbor Ising models.

2.3.1 General case

Unlike molecular simulations, which provide configurations in real space, transfer matrices are probabilistic objects. Structural observables commonly accessible in the former may thus not as easily be obtained from the latter. For instance, although the pair correlation, $g(x)$, can be computed by (inverse) Fourier transforming the structure factor [30], this approach is not straightforwardly generalizable to many other structural observables. To sidestep this difficulty equilibrium states can be *planted* for subsequent analysis from the eigenvectors of these matrices. The marginal probability $P(a)$ (or $P(a)\delta a$ in off-lattice models) of a state a in equilibrium configurations is indeed given by

$$P(a) = \frac{u_0^{-1}(a)u_0(a)}{\sum_i u_0^{-1}(i)u_0(i)}, \tag{2.42}$$

and the conditional probability that, given a state of a, the subsequent state is a', $P(a'|a)$ (or $P(a'|a)\delta a'$ in off-lattice models) is

$$P(a'|a) = \frac{u_0^{-1}(a)T_{aa'}u_0(a')}{\sum_i u_0^{-1}(a)T_{ai}u_0(i)} = \frac{T_{aa'}u_0(a')}{\lambda_0 u_0(a)}. \tag{2.43}$$

Once the leading eigenvector of the transfer matrix is known, we can propagate an equilibrium configuration of arbitrary size by the following algorithm.

1. Generate a "starting" configuration according to Eq. (2.42) by initializing a cumulative probability distribution array $Q(a)$ based on the marginal probability $P(a)$ such that

$$Q(a) = \sum_{i=1}^{a} u_0^{-1}(i) u_0(i) \sim \sum_{i=1}^{a} P(i), \tag{2.44}$$

for indexed states $a = 1, ..., n$, and $Q(0) = 0$.

2. Generate a uniformly distributed random variable $\gamma \in [0, 1)$ and choose a state with index a such that $Q(a-1) \leqslant \gamma Q(n) < Q(a)$.

3. Initialize another cumulative probability distribution array $Q(a'|a)$ for the conditional probability $P(a'|a)$, such that

$$Q(a'|a) = \sum_{i=1}^{a'} T_{ai} u_0(i) \sim \sum_{i=1}^{a'} P(i|a), \tag{2.45}$$

for indexed states $a' = 1, ..., n$, and $Q(0|a) = 0$.

4. Generate a random variable γ again and choose the subsequent state a' from $Q(a'-1|a) \leqslant \gamma Q(n|a) < Q(a'|a)$.

5. Propagate subsequent states by setting $a \leftarrow a'$ and repeating steps 3 and 4.

Remarks on continuum space model

The above algorithm assumes the microscopic state a is a discrete variable, which is the case of the Ising models. When a denotes a continuous variable in off-lattice models, the sampling must then be interpolated. Specifically, a and a' are found by $a = f(\gamma Q(n))$ and $a' = f(\gamma Q(n|a)|a)$, where $f(\cdot)$ and $f(\cdot|a)$ are interpolation functions that map $Q(a) \mapsto a$ and $Q(a'|a) \mapsto a'$, respectively. For sufficiently large n, the choice of interpolation method does not significantly affect the result, and for the q1D hard disk model considered a simple cubic interpolation scheme suffices.

2.3.2 Compressed transfer matrices

While the algorithm can be straightforwardly implemented for the ordinary transfer matrices introduced in Sec. 2.1, moderate adaptation needs to be done for the compressed transfer matrices introduced in Sec. 2.2. Namely, we need to transform the equivalent states $[b]$ to the spin states a.

Assume we have obtained a sequence of $[b_0], [b_1], ...$ from the planting algorithm. The spin states can be recovered as follows:

1. Randomly pick up a spin layer state $a_0 \in [b_0]$,

2. For each $i = 1, 2, ...,$ computing the inter-layer interaction between a_{i-1} and $a' \in [b_i]$, namely, assigning the Boltzmann weight to every a',

$$w(a_{i-1}, a') = \exp(-\beta V(a_{i-1}, a')), \tag{2.46}$$

   then randomly choose one state with th probability proportional to $w(a_{i-1}, a')$ as a_i.

3

Physical property investigation

In this chapter, I present the physics findings of the frustrated next-nearest-neighbor Ising models obtained from the numerical TM approach. For each model considered, I first briefly review its expected physical behaviors, and then aim to resolve the ambiguities with TM results. Note that, except for the ANNNI model, I discuss only the case of $h = 0$ (in absence of external field).

3.1 ANNNI model

3.1.1 Overview

As one of the most extensively studied Ising extension, the two dimensional ANNNI model has been considered by different approximation methods, including the Hamiltonian limit [40–42], the free fermion approximation [43], high-temperature series expansion [44], and others [25, 45–48]. The major debate on this model is the existence of the incommensurate (IC) phase. For instance, the cluster variational method (CVM) gives a fairly wide range of IC phase [45] while a density variation renormalization group (DMRG) study [48] suggests the IC phase only exists over an infinitesimal temperature range. As a result, although the physics of both the

small frustration regime and the energetic ground states has long been solved, that of the finite temperature-strong frustration regime has not. Between the standard high-temperature paramagnetic phase and low-temperature modulated antiphase, a floating IC phase likely intercalates. A field-theoretic treatment suggests that this critical phase—if it exists—is of the Kosterlitz-Thouless (KT) type, and thus belongs to the XY universality class [49, 50]. Numerical validation, however, has remained elusive, as has whether the IC phase persists at large frustrations or disappears at a Lifshitz point [47]. Equilibrium Monte Carlo simulation approaches have reported different high and low transition temperatures [27, 28, 51, 52], T_{c1} and T_{c2}, respectively. Non-equilibrium relaxation simulations suggesting that the IC phase has but an infinitesimal width [26, 53] have since been refuted [27]. The proposed reentrance of the IC phase around the multiphase point [45, 46] also remains to be confirmed. Because these features are central to our understanding of the floating IC phase in microphase formers, clarifying their nature is particularly important.

3.1.2 Signatures on incommensurability

We first investigate the behavior of the leading and subleading correlation length using both ${}_{\perp}$TM and ${}_{\parallel}$TM in order to detect the signature on the IC phase, and to design the criteria for extrapolating transition temperatures. These results will also serve as reference for other models. In order to probe further the existence of a critical IC (or floating) phase, we also compare the domain wall free energy, using a scheme first proposed for the DMRG approach [48].

Comparing the leading correlation length, ξ_1, obtained from ${}_{\perp}$TM and ${}_{\parallel}$TM highlights the anisotropic nature of the model (Fig. 3.1). In particular, as T increases results from ${}_{\perp}$TM decay non-smoothly due to the crossing of sub-dominant correlation lengths [Fig. 3.1(a), inset]. This phenomenon, which generically accompanies a structural crossover [32], here bespeaks a stepwise change in the modulation period,

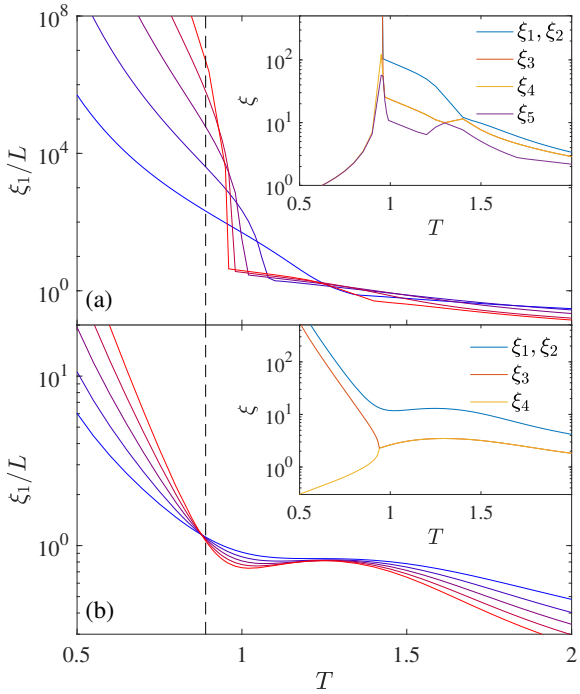

FIGURE 3.1: Leading correlation length for the ANNNI model with $\kappa = 0.6$ in (a) $_{\perp}$TM, $L = 8, 12, ..., 24$ and (b) $_{\parallel}$TM, $L = 8, 10, ..., 16$, from blue to red. The ordering transition position, $T_{c2} = 0.89(1)$ (dashed line) is given as reference. Results from $_{\parallel}$TM converge more smoothly and cleanly to the thermodynamic limit. Inset: First few leading correlation lengths in (a) $_{\perp}$TM for $L = 24$ and (b) $_{\parallel}$TM for $L = 16$. Eigenvalue crossings in the former leads to a complex T dependence of the corresponding ξ_1.

as we will show later. For $L = 24$, for example, two distinct steps can be identified, both involving $\xi_1 = \xi_2$ (that are associated with doubly degenerate eigenvalues) crossing the subleading ξ_3 and ξ_4. These features, however, complicate the evolution of ξ_1, and hence hinder the local exponent analysis and the identification of the IC phase [19, 20, 22]. By contrast, results for $_{\parallel}$TM evolve smoothly with T. The non-monotonic growth of $\xi_1 = \xi_2$ (associated with complex conjugate eigenvalues) at intermediate T can thus be construed as a signature of the critical IC phase, and its boundaries can then be extrapolated by finite-size scaling, as we will show in the next subsection. In addition, the subleading correlation lengths ξ_3, ξ_4 are found to merge at the $\langle 2 \rangle$-to-IC phase transition temperature, $T_{c2}(L)$.

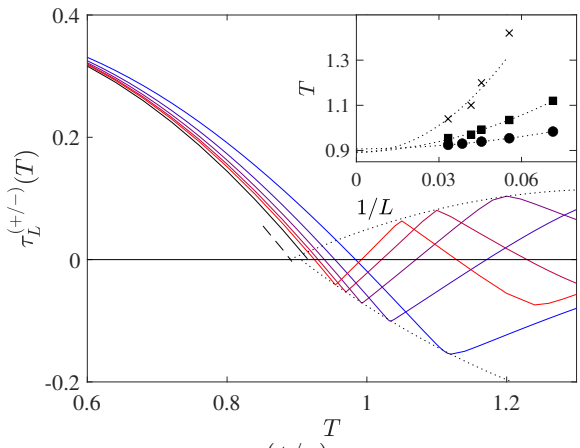

FIGURE 3.2: Domain wall free energy $\tau_L^{(+/-)}(T)$ for the ANNNI model with $\kappa = 0.6$ from ${}_{\perp}$TM with $L = 14, 18, ..., 28$ from blue to red lines. The extrapolation of $\tau^{(+/-)}(T)$ from Eq. (3.2) with the scaling expected for the antiphase, $B = 2$ (black solid line), vanishes at $T = 0.91(1)$. The extrapolation with the scaling expected for the critical point, $B = 1$ (dashed black line), gives $T_{c2} = 0.89(1)$. Both are numerically consistent with previous estimates. Inset: extrapolating the position of local peaks (crosses), valleys (squares) and the first zeros (circles) is consistent with T_{c2} (dotted lines, guides for the eye).

The stepwise change in the modulation period can also been identified from the domain-wall free energy obtained from comparing two systems under different boundary conditions [54],

$$\tau_L^{(+/-)}(T) = L[f_L^{(+/-)}(T) - f_L^{(+/+)}(T)]\sigma_L, \tag{3.1}$$

where $f_L^{(+/-)}$ (or $f_L^{(+/+)}$) are the free energy of a system fixing $s_1 = +1$ and $s_L = -1$ (or $+1$), respectively, and $\sigma_L = \pm 1$ in that the ground state $\tau_L^{(+/-)}$ is positive. In the $\langle 2 \rangle$ phase, and for modulations congruent with $L \mod 4 \equiv 2$, the expected finite-size scaling is [54]

$$\tau^{(+/-)}(T) - \tau_L^{(+/-)}(T) \sim L^{-B}, \tag{3.2}$$

where the exponent is observed to be $B = 2$ in the $\langle 2 \rangle$ phase [54], but pre-asymptotic corrections grow upon approaching the critical temperature, T_c, whereat scaling theory gives $B = 1$ [55].

Following Ref. [48], we first fit the results with $B = 2$ and extrapolate the thermodynamic $\tau^{(+/-)}(T)$ over a broad range of $0.6 < T \lesssim T_{c2}$. The result is fully consistent with the former study, predicting $T_{c2} = 0.91(1)$ (vs 0.907 in Ref. [48]). Alternatively, setting $B = 1$ (the expected critical scaling) gives $T_{c2} = 0.89(1)$. The two estimates thus differ only marginally, and are both consistent with recent predictions for the transition [22, 28].

For $T > T_{c2}$, $\tau_L^{(+/-)}(T)$ oscillates around 0, suggesting that the modulation period varies with T, a clear signature of the IC phase. Extrapolating the first peak and valley further suggests that these oscillations coalesce at T_{c2} and thus vanish in the thermodynamic limit $L \to \infty$. The zigzagging behavior weakens at larger κ yet the smoother oscillations around 0 are still observable at large L for $\kappa \gtrsim 1.5$. Such oscillatory yet vanishing free energy difference for the $(+/+)$ and $(+/-)$ boundary conditions supports the floating IC phase scenario, which is consistent with the DMRG results [48] obtained for much larger systems (10^2 vs $L \sim 10^1$).

3.1.3 Phase diagram for $h = 0$

We then consider more detailly the results from the $_\perp$TM route in absence of an external field (Fig. 3.3). For $\kappa < 1/2$, energy curves for different L robustly cross at a well-defined critical point $T_c(\kappa)$. For the Ising, $\kappa = 0$, limit $u(T_c)$ is perfectly invariant with L [56, 57], and for $0 < \kappa \lesssim 1/2$, small systems with $L \lesssim 10$ exhibit a correction of at most 0.1%. From this identification of $T_c(\kappa)$ we confirm that the heat capacity peak, $c(T^*; L)$, grows logarithmically with system size in this regime (Fig. 3.3(a) inset), as expected for systems in the Ising universality class.

For $\kappa \gtrsim 1/2$ a markedly different behavior is observed. As in simulations [52], $u(T)$ displays pronounced steps, thus giving rise to sharp heat capacity peaks [Fig. 3.3(b)]. Extrapolating the lowest peak temperature for $\kappa = 0.6$ using a quadratic form in $1/L$ gives a thermodynamic limit, $1/L \to 0$, transition temperature consistent with re-

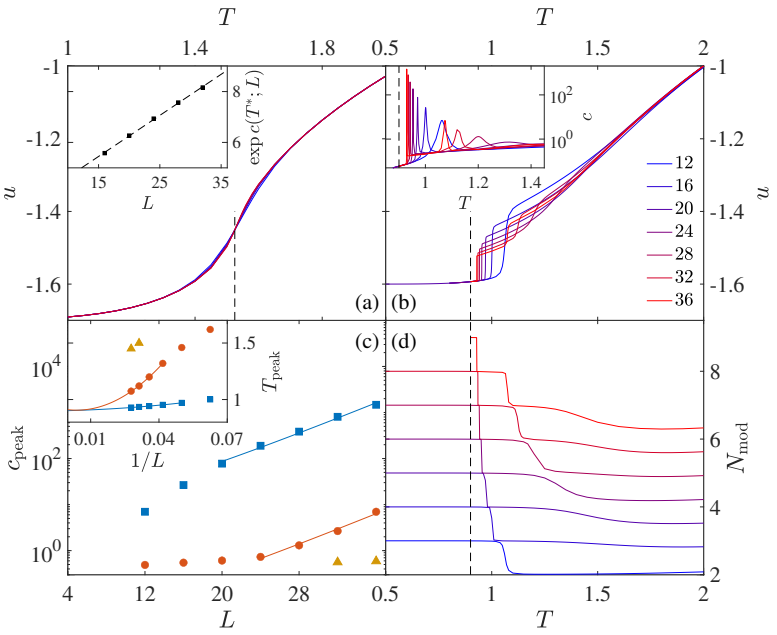

FIGURE 3.3: Thermodynamic and structural observables of the ANNNI model from $_{\perp}$TM. Evolution of the energy for (a) $\kappa = 0.3$ and (b) 0.6 with corresponding phase transition temperature estimates, T_{c} and T_{c2}, respectively (dashed lines). Insets: for the former, the heat capacity peak, $c(T^*;L)$, grows logarithmically with system size; for the latter, the heat capacity curves present distinct peaks that sharpen with L. For $\kappa = 0.6$: (c) the peak height of the lowest temperature peak, $c(T^*;L)$, grows exponentially with system size. (Inset) Extrapolating T^* with a quadratic form in $1/L$ suggests $T_{\mathrm{c2}} = 0.90(1)$, and the second peak is projected to merge with the first as $1/L \to 0$. (d) The number of modulation blocks on a layer N_{mod} correspondingly decreases stepwise with T.

cent numerics for T_{c2} [28]. At first glance, these sharp features suggest a standard first-order transition [58, 59], but the step height scales as $1/L$ (not shown), and is thus projected to vanish in the thermodynamic limit. Confusingly, the peak height of the specific heat nonetheless scales exponentially, $c(T^*;L) \sim \exp(aL)/L$ (up to $c \geqslant 10^3$) (Fig. 3.3(c)), i.e., faster than any power-law. These observations are in fact reminiscent of the Pokrovsky-Talapov transition scenario [60]. In $d = 2$, this second-order transition is expected to have heat capacity exponents $\alpha = 1/2$ and $\alpha' \to \infty$ from the floating IC and commensurate $\langle 2 \rangle$ phases, respectively [61]. Although the first scaling has long been validated from the square-root singularity of the modula-

tion wavenumber [47, 48, 51], limited simulation accuracy prevented confirming the second [52]. The exponential growth of the heat capacity peak obtained by the TM formalism completes its characterization.

Observations in the vicinity of $T \geqslant T_{c2}$ further validate the nature of the IC phase. As L increases, multiple heat capacity peaks emerge, accompanied by a stepwise evolution of the energy u and by a quantization of the number of modulation layers, N_{mod} (Fig. 3.3(b, d)). The second heat capacity peak that emerges for $L \geqslant 24$ also grows exponentially with L, and is projected to merge with the first peak as $1/L \to 0$ (Fig. 3.3 (c) inset); a third peak similarly appears for $L \geqslant 32$. For ${}_{\perp}$TM, the modulation wavenumber $q = N_{\mathrm{mod}}/L$, also decreases stepwise with T and the step height scales as $1/L$. In other words, at finite L the allowed modulations are separated by sharp crossovers, but as $1/L \to 0$ infinite commensurate phases are separated by infinitesimal temperature intervals. Each of these steps can be viewed as a "phase transition" of infinitesimal singularity, a hallmark of the persistent criticality of the floating IC phase.

As temperature increases, the floating IC to paramagnetic phase transition at T_{c1} leaves no thermal signature, as expected of a KT-type transition. Certain observables used for identifying T_{c2}, such as the wavenumber q and the domain free energy, thus exhibit no signature at T_{c1} [48]. To determine T_{c1}, we instead investigate the correlation length ξ_1 in ${}_{\parallel}$TM. Specifically, following the finite-size analysis proposed in Ref. [19], we define

$$Y_L = \frac{\log[\xi_1(L+1)] - \log[\xi_1(L-1)]}{\log(L+1) - \log(L-1)}, \tag{3.3}$$

which is the finite-L (effective or local) critical exponent for ξ_1, i.e., $\xi_1 \sim L^{Y_L}$. Because the thermodynamic limit of this quantity gives the anisotropic scaling exponent, i.e.,

$\lim_{L\to\infty} Y_L = \theta$ [62], different thermodynamic scenarios can be discerned:

$$\begin{cases} \text{in the ordered phase,} & Y_L \to \infty, \\ \text{in the disordered phase,} & Y_L \to 0, \\ \text{in the critical phase, or at } T_c, & Y_L \to \text{cnst} > 0. \end{cases}$$

Reference [19] also proposed extracting the modulation wavenumber q directly from the angular argument of the subleading eigenvalue, i.e., $q = |\arg(\lambda_1)|/2\pi$. This quantity brings about another local exponent, Z_L, which characterizes the convergence to the ground state modulation,

$$Z_L = -\frac{\log[\delta q(L+1)] - \log[\delta q(L-1)]}{\log(L+1) - \log(L-1)}, \tag{3.4}$$

where $\delta q = |q - q(T=0)|$, and similarly,

$$\begin{cases} \text{in the commensurate phase,} & Z_L \to \infty, \\ \text{in the IC phase,} & Z_L \to 0, \\ \text{at the IC transition or disorder line,} & Z_L \to \text{cnst} > 0. \end{cases}$$

Without loss of generality, we here consider results for $\kappa = 0.6$. Figure 3.4(a) shows the non-monotonic evolution of Y_L with T. Multiple crossing points (T_{low}, T_{mid} and T_{high}) as well as local extrema (T_{min} and T_{max}) can then be identified, in addition to the crossing point in Z_L, denoted T_Z (Fig. 3.4(c)). The finite-L scaling of these characteristic temperatures numerically determines the transition temperatures as well as the corresponding θ (Fig. 3.4(e, f)). In Ref. [19, 62], the floating IC phase could be loosely bound by T_Z and T_{high}; here, thanks to a vastly larger range of L being accessible, more characteristic temperatures can be analyzed, thus refining numerical estimates and clarifying the underlying physics.

To extract thermodynamic information, we consider again a quadratic fit of these characteristic temperatures with $1/L$. Although this choice arbitrarily assumes a critical scaling of L^{-t} with $t = 1$—no theoretical estimate of t is known—it nevertheless

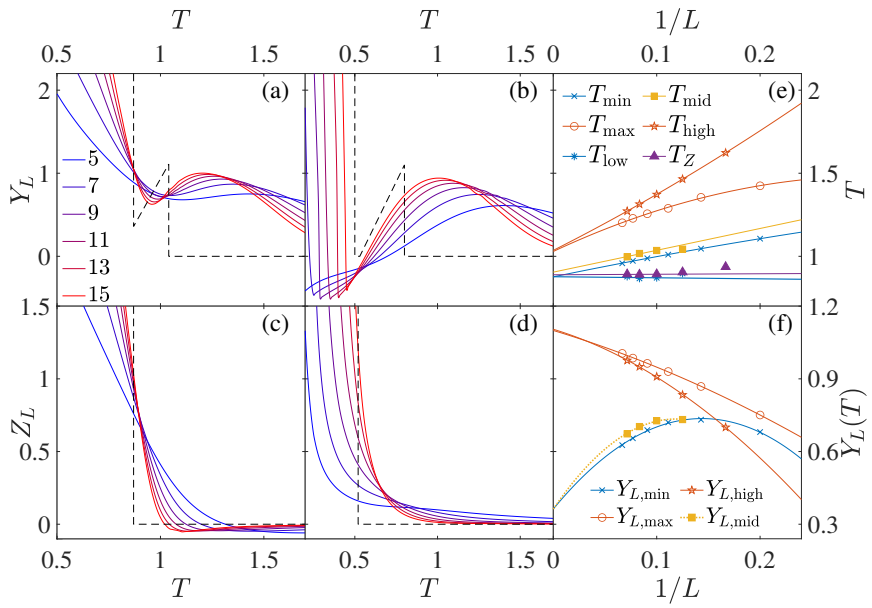

FIGURE 3.4: Correlation length analysis from $_{\parallel}$TM. Local exponents (a, b) Y_L and (c, d) Z_L for $\kappa = 0.6$ and 0.49, respectively. For $\kappa = 0.6$: (e) the two characteristic temperatures extracted from Y_L and Z_L (see text for details) coincide at T_{c1} and T_{c2}, respectively, as $1/L \to 0$; (f) the critical exponents Y_L also coincide at these temperatures. In (e) and (f), solid lines are quadratic fits (or linear fits if only three data points are available). The dotted line in $Y_{L,\text{mid}}$ is purely qualitative because of the limited number of available data points. The thermodynamic behavior of Y_L and Z_L, extracted from panels (e) and (f), are reported in (a-d) (dashed lines).

leads to a good convergence of the characteristic temperatures in the thermodynamic limit. $T_{\text{low}}, T_{\text{mid}}$, $T_{\min}$ and T_Z all coincide to $T_{c2} = 0.89(1)$, consistent with the $_{\perp}$TM analysis, and $T_{\max}$ and T_{high} both coincide at $T_{c1} = 1.04(1) > T_{c2}$. This second temperature, however, markedly differs from the two most recent simulation estimates, $T = 1.16(1)$ [27] and 1.27 [52]. (Earlier theoretical estimates vary even more, from $T_{c1} \approx T_{c2}$ [48, 53] to 1.64 [45].) Because finite-size corrections and equilibration difficulties in simulating this regime are notoriously pronounced, such discrepancy is not particularly surprising. The good agreement between multiple characteristic temperatures and the small curvature of the fits (suggestive of a relatively small pre-asymptotic correction) tend instead to support our estimate. As a further test of the scenario $T_{\text{high}} = T_{c1} = T_{c2}$, we note that the extrapolated $T_{\text{high}}(L \to \infty | \kappa = 0.6)$

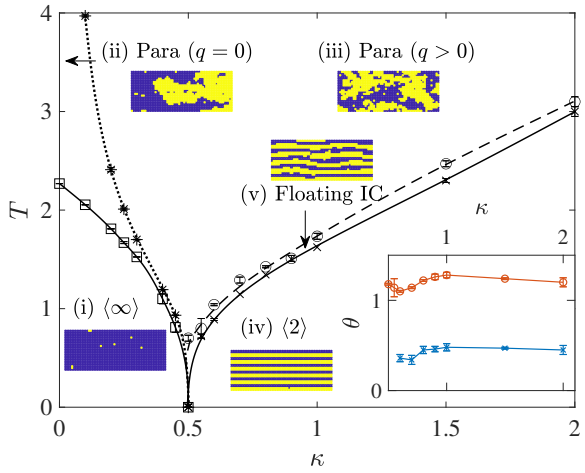

FIGURE 3.5: Phase diagram for the two-dimensional ANNNI model with $h = 0$. The TM approach provides phase boundaries for the ferromagnetic $\langle\infty\rangle$-paramagnetic (squares), commensurate antiphase $\langle 2\rangle$-floating IC (crosses), and paramagnetic-floating IC (circles) transitions. The disorder line (asterisks) subdivides the paramagnetic phase in two regimes with $q = 0$ and $q > 0$ modulation wavenumbers. Configuration snapshots generated by planting use blue and yellow pixels to denote $+1$ and -1 spins, respectively. (Inset) Extrapolated exponents at the boundaries of the floating IC phase, $\theta(T_{c1}; \kappa)$ (orange) and $\theta(T_{c2}; \kappa)$ (blue). Error bars denote the range of the extrapolated results obtained from different characteristic temperatures (see Fig. 3.4(f)). Lines are guides to the eyes.

reaches a minimum of 1.00 for $t = 0.75$, still well above T_{c2}. Interestingly, the DMRG study that supports this scenario [48] was conducted with ${}_{\perp}$TM. A DMRG formalism with ${}_{\parallel}$TM may also locate T_{c1} differently and more robustly, although the confounding effect of other approximations cannot be excluded. In any event, results of our exact transfer matrix treatment as well as recent extensive simulations [27] strongly support $T_{c1} > T_{c2}$.

The distinctiveness of the two characteristic temperatures suggests that θ monotonically increases with T for a fixed κ in the floating IC phase. Extrapolating Y_L at different characteristic temperatures, namely $Y_{L,\max}$, $Y_{L,\text{high}}$ and $Y_{L,\min}$, $Y_{L,\text{mid}}$ (as in Fig. 3.4(f)), provides approximations for $\theta(T_{c1}; \kappa)$ and $\theta(T_{c2}; \kappa)$, respectively. These exponents vary remarkably little with κ (Fig. 3.5 (inset)). The two distinct transition temperatures thus likely persist as κ increases, even though a quantitative distinction

between the two transition temperatures by finite-size scaling is here only feasible up to $\kappa \approx 2$. The non-monotonic behavior of Y_L that gives rise to this behavior in the thermodynamic limit hence lends support to the floating IC phase surviving as $\kappa \to \infty$, and goes against the finite-κ Lifshitz point scenario [40, 63].

For κ slightly smaller than 1/2, a distinct feature emerges in Y_L. For example, for $\kappa = 0.49$ a narrow disordered region with $Y_L \to 0$ is squeezed between the ferromagnetic phase and the floating IC phase (Fig. 3.4(b)). For $\kappa < 1/2$, a disorder line subdivides the disordered regime [47, 64], where the correlation length exhibits a kinked local minimum. Given that the disorder line identified by the fixed point of Z_L (Fig. 3.4(d)) extends down to the multiphase point at (κ=1/2,T=0) [45, 65], we conclude that the floating IC and Ising ferromagnetic phases never meet for $T > 0$. This analysis thus confirms the reentrance of the floating IC phase in this regime, as various theoretical treatments have proposed [45, 46]. The disorder line for decreasing $\kappa < 1/2$ is also found to be asymptotically tangent to $\kappa = 0$ as $T \to \infty$, instead of $\kappa = 0.25$, as was previously suggested [45]. Combining these various observations provides a complete quantitative phase diagram for the two-dimensional ANNNI model at $h = 0$ (Fig. 3.5).

3.1.4 Phases diagram for $h > 0$

The ANNNI model in lattice-gas representation can be viewed as a minimal model for lamellar microphases. For this model, as in generic SALR microphase formers [66], at low T and small κ a coexistence regime around $h = 0$ separates the condensed (-1 spins dominated) and gas ($+1$ spins dominated) phases, while for $\kappa > 1/2$ lamellar microphases replace macroscopic phase separation. Increasing h then depresses the $\langle 2 \rangle$ melting temperature down to $T \to 0$ at $h^* = 2\kappa - 1$ [67]. Figure 3.6 presents results for $\kappa = 0.6$ (for which $h^* = 0.2$). At large h the ground state is a saturated paramagnetic phase without modulations. Although this regime

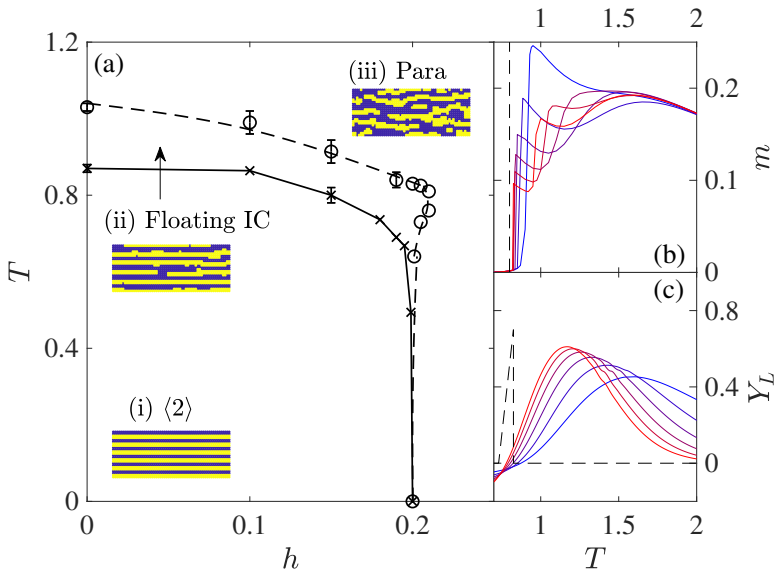

FIGURE 3.6: (a) Phase diagram for the two-dimensional ANNNI model with $\kappa = 0.6$ and varying h. Crosses denote the transition between the antiphase $\langle 2 \rangle$ and the floating IC phase, and circles that between the floating IC phase and the paramagnetic phase. Snapshots are obtained as in Fig. 3.5. (b) Evolution of the magnetization per spin with temperature for $h = 0.15$ obtained from ${}_{\perp}$TM with $L = 12 \ldots 32$, from blue to red. Note the clear jump in magnetization at T_{c2} (dashed line). (c) Y_L for $h = 0.205$ obtained from ${}_{\parallel}$TM with $L = 5 \ldots 15$, from blue to red. Extrapolating characteristic temperatures (as in Fig. 3.4) shows that the floating IC phase emerges at intermediate T as $Y_L > 0$ (dashed line).

exhibits spin configurations akin to those of a ferromagnetic phase, its correlation length is finite. At smaller h—as for $h = 0$—a floating IC phase intercalates between the commensurate $\langle 2 \rangle$ and the paramagnetic phases. The ${}_{\perp}$TM route confirms that the magnetization per spin, m, remains null in the $\langle 2 \rangle$ phase and jumps (as does u) at the transition [Fig. 3.6(b)]. By contrast, spin layers preferentially align with the external field in the floating IC phase, which leads to the magnetization increasing stepwise with temperature. At yet higher temperatures, in the paramagnetic phase m again decreases as entropy increasingly dominate. Slightly above h^* the floating IC phase reenters, in a way reminiscent of the $J_1 - J_2$ model [68]. The behavior of the local exponent Y_L, which crosses at the lower-T boundary of the IC phase and peaks at the higher-T phase boundary [Fig. 3.6(c)], is also similar to the reentrance

in Fig. 3.4(b). Extrapolating these special temperatures gives the phase boundaries in Fig. 3.6(a). Note that for $h \gtrsim 0.22$, the order of the extrapolated lower and higher temperature boundary of the IC phase changes and $Y_L(T_{c1})$ is projected to vanish. The thermodynamic floating IC phase then terminates, even though strong finite-size echoes of it appear to persist.

3.2 DNNI model

3.2.1 Overview

The energetic ground state of the DNNI model in absent of external field ($h = 0$) is ferromagnetic for $\kappa < 1/2$ and striped with $\langle 1 \rangle$ for $\kappa > 1/2$ (of period 2, $\uparrow\downarrow$). In both cases, melting leads directly to a disordered phase, but whether or not the transition remains first-order in nature around $\kappa = 1/2$ has long been debated. The putative first-order regime indeed appears to narrow as the quality of numerical studies improves. Predictions for a Potts point dividing the weakly-first-order from the continuous transition vary from $\kappa^* \simeq 0.9$ [69, 70], 0.67(1) [21, 71] to $\simeq 0.54$ [72].

For $\kappa < 1/2$, it has generally been assumed that the transition is part of the Ising universality class, but recent cluster mean-field approximation and effective-field theory study suggest that a narrow first-order transition regime might also be found at $\kappa \lesssim 1/2$ [21, 73]. Several simulation studies further suggest a nonzero transition temperature at $\kappa = 1/2$ proper, i.e., $T_c(\kappa = 1/2) > 0$ [74–76], in marked contrast to prior works [77–81]. Because theoretical approximations behave irregularly around $\kappa \lesssim 1/2$ [82], however, a conclusive assessment has thus far remained out of reach.

In the next, we first compare the correlation length, internal energy and domain wall free energy results with those of the ANNNI model in the previous Section. We then attempt to resolve these phase ambiguities.

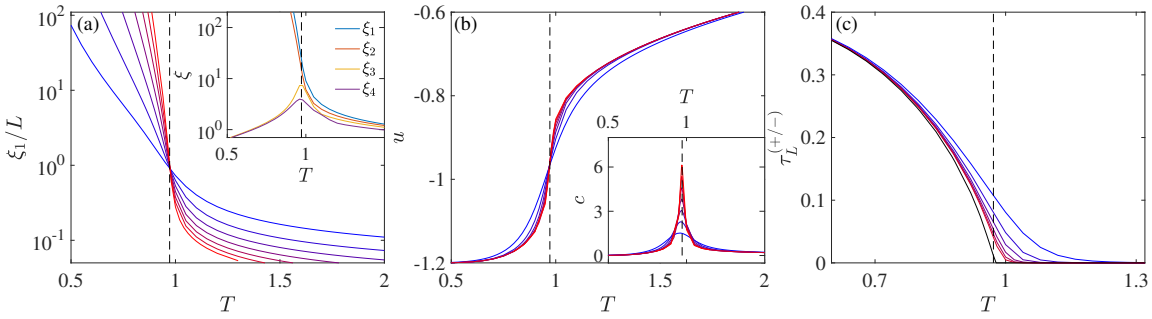

FIGURE 3.7: Finite-size results for various observables of the DNNI model with $\kappa = 0.6$, for which $T_c = 0.971(1)$ (dashed vertical lines) for $L = 8, 12, ..., 32$ (from blue to red lines). (a) The leading correlation length cross at single fixed point for all L. Inset: the first few leading correlation lengths for $L = 24$. No correlation length splitting or crossing is observed. (b) Energy per spin u and (Inset) specific heat c per spin. Both ξ_1/L and u present a fixed point and c peaks sharply at T_c. (c) Domain wall free energy for $L = 14, 18, ..., 28$ from blue to red lines. The extrapolated $\tau^{(+/-)}$ from Eq. (3.2) (black solid line) vanishes at T_c (dashed line).

3.2.2 Thermodynamic Observables

The evolution of ξ_1 for the DNNI model is smooth and monotonic (see, e.g., Fig. 3.7(a)); no eigenvalue crossing or splitting is observed. Unlike the ANNNI model, which presents an algebraic growth, $\xi_1 \sim L^{\theta}(T)$, over a temperature range [19, 22], the DNNI model displays an algebraic scaling only at a single temperature. Also, the anisotropy exponent is then $\theta = 1$ ($\xi_1/L \approx$ const), as expected for models with isotropic interactions [83]. The crossing point of ξ_1/L further provides an accurate estimate of T_c. Other robust estimators include the crossing point of the internal energy and the peak of the specific heat [Fig. 3.7(b)]. Because the finite-L transition temperature $T^*(L)$ identified by these estimators changes little with L, transition estimates can often be identified with up to five significant digits [21]. (Around $\kappa = 1/2$, the situation is more complex, as discussed below.)

We also evaluate the domain wall free energy using Eq. (3.1) [Fig. 3.7(c)]. As expected, $\tau_L^{(+/-)}$ follows the finite-size scaling of Eq. (3.2) in the ordered striped phase. For $B = 1$, it is extrapolated to vanish at T_c. (The ~ 0.01 deviation from

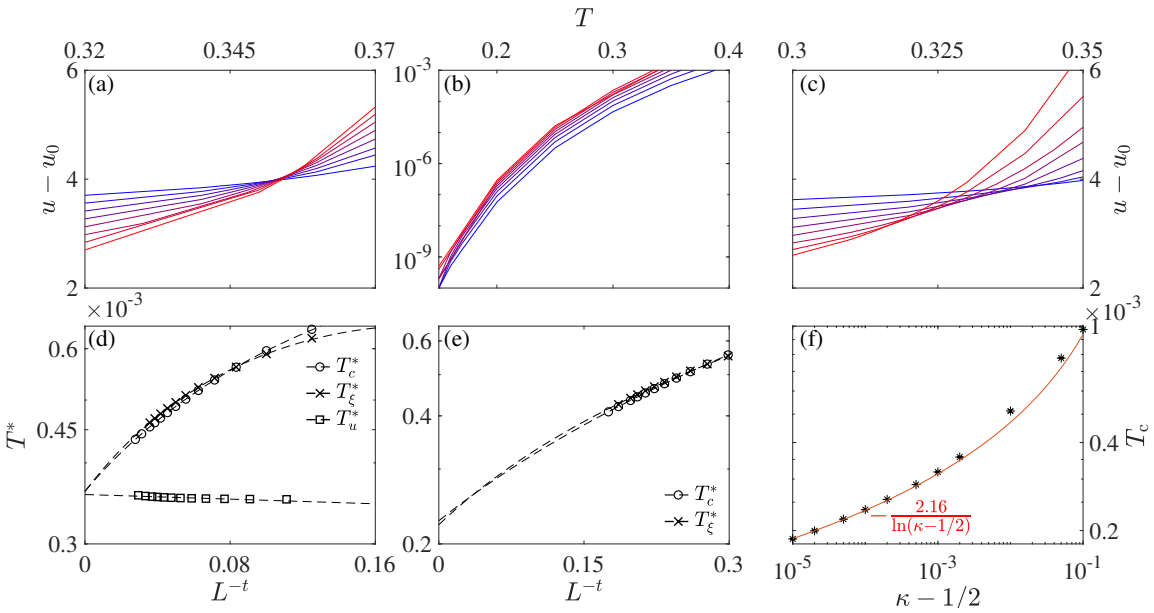

FIGURE 3.8: Phase transition determination around $\kappa = 1/2$. (a-c) Internal energy above the ground state, $u_0 = -(1 + 2|\kappa - 1/2|)$, for $\kappa = 0.502, 1/2, 0.498$. (d, e) extrapolation of the temperature via different estimators indicated in legends (see text for detail) for $\kappa = 0.502$ and $1/2$, respectively. Dashed lines are fitted using Eq. (3.5) with empirical exponent $t = 1$ and 0.486, respectively (quadratic fits are used for $T_c^*(L)$ and $T_\xi^*(L)$). The results from different estimators are mutually consistent; and for (e) it reproduces Ref. [75]. (f) T_c vanishes logarithmically as $\kappa \to 1/2^+$.

T_c is likely due to pre-asymptotic corrections.) Unlike in Fig. 3.2, here no signature of stepwise oscillation is observed for $\tau_L^{(+/-)}(T > T_c)$. This monotonic evolution is robust for various κ both below and above $1/2$. The incommensurate phase—or its finite L echo—is thus clearly absent in the DNNI model.

3.2.3 T_c determination

Knowing the expected behaviors for various estimators at the phase transition, we now quantitatively evaluate T_c. In particular, we wish to determine whether $\lim_{\epsilon\to 0} T_c(1/2 + \epsilon) = 0$. As shown in Fig. 3.8(a,c), a crossing point in T-u curve is detected for both side of $\kappa = 1/2 \pm 0.002$, but is absent right at $\kappa = 1/2$ down to numerical accuracy (in practice, $\sim 10^{-10}$) [Fig. 3.8(b)]. The crossing thus seemingly

takes place at $T = 0$, as does the phase transition.

More systematically, we note that for $\epsilon > 0$, $T_u^*(L)$ barely shifts with L, while for $\epsilon < 0$ significant pre-asymptotic corrections appear [see Fig. 3.8(a,c)]. We thus apply an empirical fitting form to extrapolate $T_{\rm c}$,

$$T^*(L) = T_c + AL^{-t} \tag{3.5}$$

with a fitting constant A and empirical exponent t ($t = 1$ for $\kappa > 1/2$). Note that other estimators, such as the location of specific heat and the correlation length peaks [see Fig. 3.10(c)], $T_c^*(L)$ and $T_\xi^*(L)$, provide consistent estimates [Fig. 3.8(d)], but require a quadratic correction, BL^{-2t}, to Eq. (3.5) and are thus less accurate. Thanks to the exceptionally small finite-size corrections to $T_u^*(L)$ and the high TM accuracy, $T_{\rm c}$ can be determined down to $\epsilon = 10^{-5}$ [Fig. 3.8(f)]. (For $\epsilon < 0$, however, T_u^* seemingly shifts to lower T as L increases thus the extrapolation is ambiguous.) Remarkably, the resulting transition temperature scales logarithmically as

$$T_{\rm c}(\kappa) \approx -\frac{2.16}{\ln(\kappa - 1/2)}. \tag{3.6}$$

We thus confidently conclude that $T_{\rm c}(\kappa = 1/2) = 0$.

To better understand why Ref. [75] concluded differently, we replicate their analysis in Fig. 3.8(e) (with the same $t = 0.486$), and consider $T_\xi^*(L)$ as well. Both extrapolations give $T_c(\kappa = 1/2) = 0.22(1)$, as Ref. [75] found. Previous extrapolation attempts have thus been obfuscated by the complex and significant pre-asymptotic corrections to various variables around $\kappa = 1/2$, as we will discuss next.

3.2.4 Order of transition

Another actively debated question about the DNNI model is the order of its phase transitions. In principle, this can be determined from the scaling of the peak specific heat.

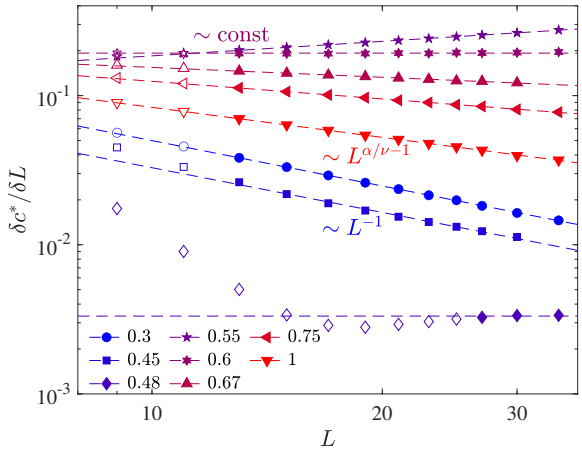

FIGURE 3.9: Finite-size scaling of the DNNI peak specific heat for various κ. $\delta c^*/\delta L \sim L^{-1}$ for the Ising-type continuous transition ($\kappa = 0.3, 0.45$); $\sim L^{\alpha/\nu-1}$ with $0 < \alpha/\nu \leqslant 1$ for the AT-type continuous transition ($\kappa = 0.67, 0.75, 1$) and is expected to approach constant for the first-order scenario ($\kappa = 0.48, 0.55, 0.6$) but the slope of the fitting line varies continuously in $0.5 < \kappa < \kappa^*$.

1. For an Ising-type continuous phase transition (expected for small κ),

$$c^*(L) \approx A \log L + c_0, \tag{3.7}$$

   c_0 denotes the *background* specific heat and A is a fitting constant.

2. For a first-order transition (expected for $1/2 < \kappa < \kappa^*$ and speculated for $\kappa^\dagger < \kappa < 1/2$),

$$c^*(L) = AL + c_0. \tag{3.8}$$

3. For an Ashkin-Teller (AT)-type phase transition (expected for $\kappa > \kappa^*$),

$$c^*(L) = AL^{\alpha/\nu} + c_0, \tag{3.9}$$

   where α is the heat capacity exponent and ν is the correlation length exponent, and $0 < \alpha/\nu \leqslant 1$. In particular, $\alpha/\nu = 1$ characterizes the Potts critical point.

To eliminate the background correction, we here consider the finite differentiate, which scales as

$$\delta c^*/\delta L = [c^*(L+1) - c^*(L-1)]/2 = AL^b, \tag{3.10}$$

with $b = \alpha/\nu - 1$ for continuous transitions and with $b = 0$ (a plateau) for first-order transitions. Results for selected κ are reported in Fig. 3.9. Fitting Eq. (3.10) gives $\alpha/\nu = -0.01(3)$ and $0.09(10)$ for $\kappa = 0.3$ and 0.45, respectively, both consistent with an Ising-type transition with $\alpha = 0$. In the (expected) weakly first-order regime $1/2 < \kappa < \kappa^*$, however, the fitting slope decreases with κ. For instance, $\kappa = 0.55$ and 0.6 give $b = 0.32(2)$ and $0.02(1)$, respectively, instead of $b = 0$ throughout. This drift, which was also reported in Monte Carlo simulations of small systems [59], suggests that pronounced finite-size corrections are a play. The TM approach thus still cannot distinguish a weakly first-order from a continuous transition, nor clearly identify κ^*. Nevertheless, the drift of α/ν observed at larger κ (e.g., $\kappa = 0.75$ and 1 give $\alpha/\nu = 0.61(2)$ and $0.33(2)$, respectively) is consistent with the AT-type transition with varying exponent [21, 71].

By contrast, the Ising-type (for small κ) and the weakly first-order transitions (speculated for $\kappa^\dagger < \kappa < 1/2$) can be distinguished more straightforwardly from the distinct $b = -1$ and 0, respectively. A clear $b = -1$ scaling persists at least up to $\kappa = 0.45$. For $\kappa = 0.48$, however, $\delta c^*/\delta L$ first decreases with L, and then grows slightly before plateauing. Although pre-asymptotic features partly obfuscate the physical picture, this trend clearly deviates from an Ising-type transition. These results are instead reminiscent of a weakly first-order transition, and thus support the theoretical speculations of Refs. [21, 73] that such a regime should exist for $\kappa^\dagger < \kappa < 1/2$ with $\kappa^\dagger \gtrsim 0.45$. (Reference [75] concluded that a continuous transition takes place for $\kappa = 0.48$, based on the absence of discontinuity in $u(T)$, but did not consider the weakly first-order transition scenario.) Interestingly, a recent the Bethe lattice computation at low connectivity suggests that such a weakly first-order transition in the vicinity of the multicritical point ($\kappa \lesssim 1/2$ in the DNNI model) is a mean-field feature [84]. This behavior thus clearly differs from the fluctuation-induced discontinuity for $1/2 < \kappa < \kappa^*$.

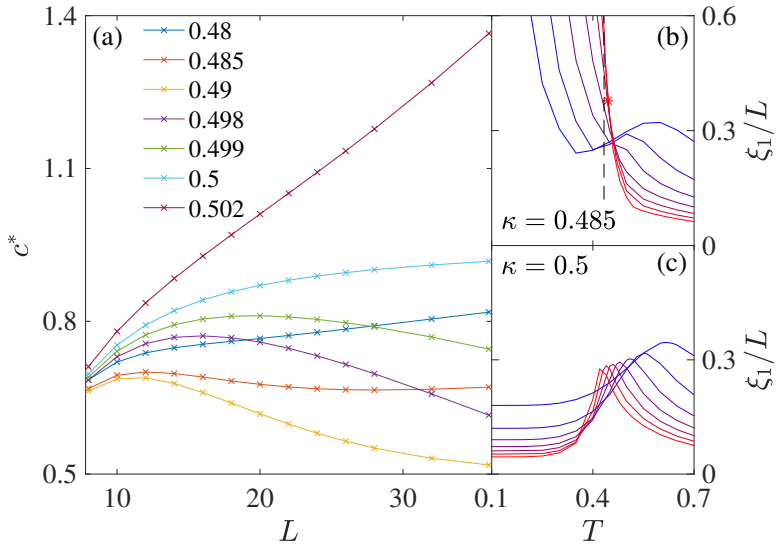

FIGURE 3.10: The DNNI model exhibits pronounced pre-asymptotic corrections around $\kappa = 1/2$: (a) peak specific heat $c^*(L)$ for various κ around 1/2; and (b, c) leading correlation length for $L = 8, 12, ..., 32$ at $\kappa = 0.485$ and 1/2 with T_c (dashed line in b). For $\kappa = 0.485$, as L grows the crossing points between subsequent ξ_1/L (asterisk between $L = 28$ and 32) approach T_c, while the local peak vanishes.

This distinction might explain the markedly different scaling properties observed in each side of $\kappa \to 1/2$ [as observed earlier in Fig. 3.8(a,c)]. Slightly above $\kappa = 1/2$, pre-asymptotic deviations are barely notable. For example, at $\kappa = 0.502$ a linear growth of $c^*(L)$ is detected already for $L \geqslant 28$, consistent with the weakly first-order transition scenario. By contrast, slightly below $\kappa = 1/2$ deviations from scaling are so pronounced that an asymptotic scaling analysis is impractical (see Fig. 3.10(a)). For instance, for $\kappa = 0.485$, $c^*(L)$ decreases at intermediate L before increasing again. From $\kappa = 0.485$ to 0.499, this pre-asymptotic behavior extends to even larger L as $\kappa \to 1/2$. Moreover, the range of small L growth extends as well, leaving but a purely monotonic growth at $\kappa = 1/2$. The evolution of ξ_1 also hints at a complex finite-size behavior for $\kappa \lesssim 1/2$. For example, for $\kappa = 0.485$, a local peak appears at small L but disappears as L increases [Fig. 3.10(b)], and then a crossing is recovered around T_c. As κ further approaches 1/2, this local peak survives for larger systems and is expected to persist for all $L \to \infty$ at $\kappa = 1/2$ [Fig. 3.10(c)]. In this limit case,

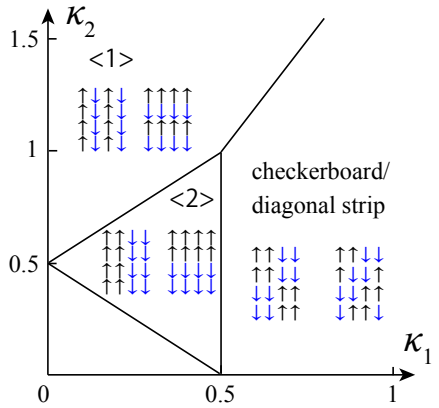

FIGURE 3.11: $T = 0$ (ground state) phase diagram for the 3NNI model

ξ_1 approaches a constant at both low and high T, but a peak persists (the effective exponent $\mathrm{d}\ln\xi_1/\mathrm{d}\ln L$ approaches 1), thus suggesting a disorder-disorder transition (albeit possibly shifting to $T = 0$ in the limit $L \to \infty$).

Note that the correlation length obtained from Monte Carlo simulations of a $L \times L$ square lattice was found to diverge exponentially as $T \to 0$ [77], which markedly differs from the ξ_1 results from ${}_{\perp}$TM. The observation of Ref. [77] is instead recovered when ${}_{/}$TM is used (its growth is similar to Fig. 3.15(e) which will be discussed in Sec. 3.4.2), thus also consistent with the picture of $T = 0$ phase transition (with diverging correlation length) but with a different finite-size scaling than ${}_{\perp}$TM.

In summary, while a signature of a first-order transition is observed at $\kappa = 0.485$, pronounced finite-size effects in various observables prevent further confirmation for $\kappa^{\dagger} < \kappa < 1/2$. We nevertheless identified a significant pre-asymptotic regime that may be confused with a continuous transition, as was previously assumed [75, 80, 85]. Particular cautious should thus be taken in future studies.

3.3 BNNNI model

3.3.1 Overview

The BNNNI model has a ferromagnetic ground state for $\kappa < 1/2$, and the transition to the high-temperature paramagnetic phase is thought to exhibit Ising universality in that regime. For $\kappa > 1/2$ the model presents two distinct energetic ground states (Fig. 3.11): 4×4 checkerboard order, or diagonal stripes of width 2. Early Monte Carlo simulations suggested that melting of these structures proceeds through a first-order transition [59], but later work found the thermodynamic evolution to be more complicated. Multiple metastable states indeed develop at intermediate temperatures [86], and a two-step transition involving a critical IC phase at $1/2 < \kappa < \kappa^*$ [20, 87–89] has been proposed. It is further unclear whether the Lifshitz point takes place at finite κ^*, or whether $\kappa^* \to \infty$. Even studies suggesting the former offer but a qualitative determination of κ^* [88].

In the next, we mainly analyze the signatures of the phase transition in the antiphase regime ($\kappa > 1/2$), in order to obtain an overall quantitative phase diagram, which has so far eluded numerical considerations.

3.3.2 Correlation length scaling

We first consider the T evolution of correlation lengths with $_{\parallel}$TM and $_{/}$TM for $\kappa = 0.6$ (Fig. 3.12). In both cases, ξ_1 evolves non-monotonically, resulting from multiple eigenvalue crossings. These features are strongly reminiscent of the ANNNI results and markedly differ from their DNNI counterparts, which suggest that a critical phase between T_{c1} and T_{c2} might be found. For $_{\parallel}$TM, a sharp local peak emerges slightly above the antiphase regime for congruent $L \bmod 4 \equiv 0$, and shifts to lower T as L increases. Quantitatively extrapolating transition temperatures from this observable is, however, not realistic given the limited range of accessible system

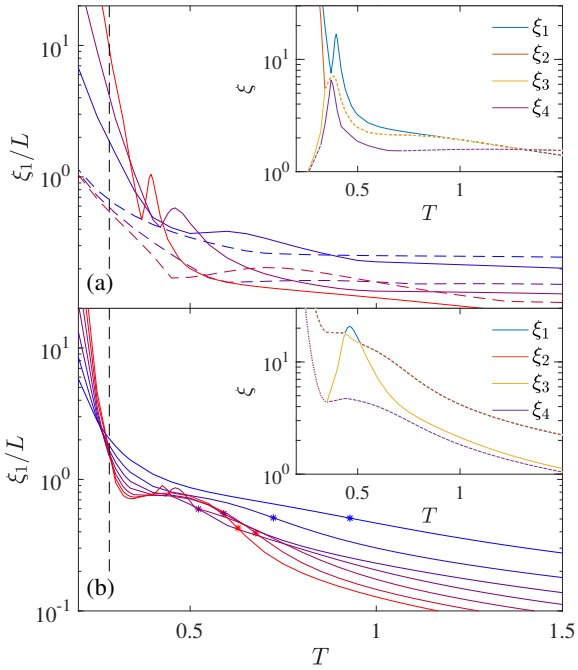

FIGURE 3.12: Leading correlation length for the BNNNI model with $\kappa = 0.6$ in (a) $_{\parallel}$TM with $L = 8, 12, 16$ (solid lines) and $L = 6, 10, 14$ (dashed lines); and (b) $_{/}$TM with $L = 8, 12, ..., 32$, from blue to red lines, respectively. Asterisks mark the turning point $T_1^*(L)$ used to extrapolate T_{c1}. Inset: the first four leading correlation lengths in (a) $_{\parallel}$TM with $L = 16$ and (b) $_{/}$TM with $L = 24$. Dashed lines denote degenerate correlation length related by complex conjugate subleading eigenvalues. Vertical dashed lines in both panels denote the transition temperature $T_{c2} = 0.283(3)$.

sizes and the size congruence constraint. By contrast, $_{/}$TM presents a much more straightforward trend. As $L \to \infty$, ξ_1/L (i) diverges in the commensurate antiphase, (ii) approaches a constant in the putative IC phase, $T_{c2} \leqslant T \leqslant T_{c1}$, and (iii) vanishes in the disordered paramagnetic phase [20, 83]. From the lowest temperature crossing points of ξ_1/L between systems of two nearby sizes, $T_2^*(L)$, we can extrapolate T_{c2} using a correction form

$$T_2^*(L) - T_{c2} = A_1 L^{-1}(1 + A_2 L^{-1}), \tag{3.11}$$

where A_1, A_2 are fitting constants. Although the scaling of the correction is not known *a priori*, the resulting extrapolation is nearly linear for all κ between 0.55 and 2, thus giving credence to this form. For $\kappa = 0.6$, in particular, fitting results from

$L = 14$ to 30 gives $T_{c2} = 0.283(3)$.

While for the ANNNI model T_{c1} can be determined from the finite-size scaling of the local exponent $Y_L = \delta \ln \xi_1 / \delta \ln L$ via the $_{\parallel}$TM approach (Eq. (3.3)), for the BNNNI model the situation is not as straightforward. Eigenvalue crossings indeed persist even in the $_{/}$TM analysis [Fig. 3.1(b)]. As a result, a bump-like peak appears in the plateau regime for $L = 24, 28$ but retreats in $L = 32$. (For $L = 32$, a second peak in ξ_3 appears but does not cross ξ_1 nor ξ_2.) In order to understand the physical origin of this effect, recall that the angular argument of this pair of complex conjugate subleading eigenvalues corresponds to the modulation period. A sharp peak thus corresponds to the presence of a real eigenvalue (wavenumber $q = \arg(\lambda_1)/(2\pi) = 0$). Because the modulation can propagate along either diagonal directions, this peak indicates that the modulation perpendicular to the TM propagation direction momentarily dominates within the relevant temperature window. Said differently, L is then commensurate with the preferred wavelength. The overall scaling trend, however, remains unaffected.

The numerical challenge of determining T_{c1} nevertheless remains. A first option is to consider the scaling of anisotropy, as for the ANNNI model [19, 22]. Although small systems display a smooth evolution [20], larger L exhibit complex oscillations. The correlation length scaling in the incommensurate phase regime is thus severely affected by the boundary condition—again possibly resulting from the interference between preferred wavelength and L—hence preventing a clear determination of T_{c1}. A second option is to consider restricting the modulation along the TM direction of propagation by examining the leading correlation length associated with a complex eigenvalue, ξ_1'. Given the smooth evolution of ξ_1' with L, it is then possible to extrapolate T_{c1}. As a finite-L echo of T_{c1}, we consider the local minimum

$$\left.\frac{\partial(\log \xi_1')}{\partial T}\right|_{T_1^*(L)} = 0, \tag{3.12}$$

which graphically corresponds to the turning point of T-log(ξ_1'/L). As L increases, $T_1^*(L)$ first decreases but the monotonic trend does not persist (e.g., $T_1^*(L = 28) > T_1^*(L = 24)$). As κ increases, both the ξ_1 plateau and its turning onset become weaker. Because eigenvalue crossing is absent for the largest L considered and $T_1^*(L)$ evolves smoothly and monotonically, a tentative extrapolation of T_{c1} using Eq. (3.11) is possible for $\kappa \geqslant 0.8$ (Fig. 3.14). We thus have that $T_{c1} > T_{c2}$, beyond the uncertainty range, up to $\kappa = 1.5$, and the signature of the critical phase is qualitatively visible up to $\kappa = 2$. This evidence marginally supports the absence of a Lifshitz point, i.e., $\kappa^* = \infty$. The ANNNI and the BNNNI models both exhibit a similar correlation length plateau which suggests that an incommensurate phase exists in the former as well. We should note, however, our T_{c1} values are tentative because similar finite-size corrections—non-monotonic trend of $T_1^*(L)$—may be observed at larger L (although less severely). Hence we also cannot completely exclude that the IC-like phase disappears in the thermodynamic limit.

3.3.3 Heat capacity evolution

We next investigate the evolution of the heat capacity. Because $_{\parallel}$TM and $_{/}$TM present different finite-size features, we consider both cases. For $_{\parallel}$TM, a sharp peak grows with L, but its temperature is marginally smaller than that of the local peak of ξ_1. Correspondingly, the internal energy grows stepwise with a decreasing step height as L increases, as observed in Monte Carlo simulations [86] and in the $_{\perp}$TM solution of the ANNNI model (Sec. 3.1.3). This behavior is consistent with a Pokrovsky-Talapov type transition, at which the heat capacity divergence is discontinuous (with scaling exponent $\alpha' \to \infty$) from the antiphase side. For $_{/}$TM, the $c(T)$ curve is multiply peaked. The lowest temperature peak is the highest, whereas higher temperature peaks grow and shift to lower T as L increases. These peaks appear to evolve toward T_{c2} [Inset of Fig. 3.13(b)], as they do as finite-L-echo of the IC phase in the ANNNI

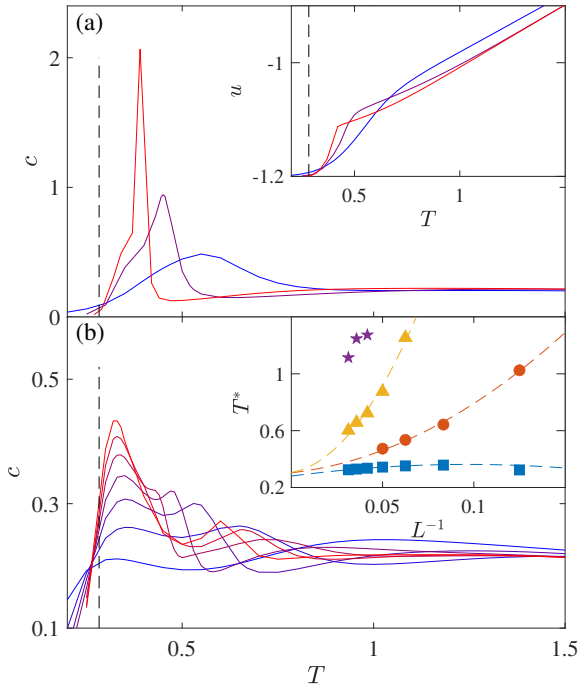

FIGURE 3.13: Specific heat for the BNNNI model for $\kappa = 0.6$ in (a) $_{\parallel}$TM for $L = 8, 12, 16$ and (b) $_{/}$TM for $L = 8, 12, ..., 32$, from blue to red. Vertical dashed lines denote $T_{c2} = 0.283(3)$. For (a), the sharp peak is located at marginally higher T than the local peak of ξ_1 [Fig. 3.12(a)] by $\sim -1\%$ differences in $L = 12, 16$. Insets of (a): energy per spin for the same systems; inset of (b): specific heat peak temperatures are extrapolated (using a quadratic fitting form) to merge at $T_{c2} \approx 0.3$ as $1/L \to 0$.

model. The analogy between the two models suggests that for $\kappa > 1/2$ the BNNNI model also undergoes a Pokrovsky-Talapov transition [60] at T_{c2}, followed by critical IC phase [50] that terminates at a KT transition at T_{c1}. The IC phase, if it exists, would then be characterized by an algebraically diverging correlation length and presents a stepwise evolution of the modulation in finite systems.

3.3.4 Phase diagram

Combining the correlation length and heat capacity results offers a consistent solution of the phase behavior of the BNNNI model (see Fig. 3.14). The simple ferromagnetic regime at $\kappa < 1/2$ presents an Ising-type transition at T_c, as identified by ξ_1/L

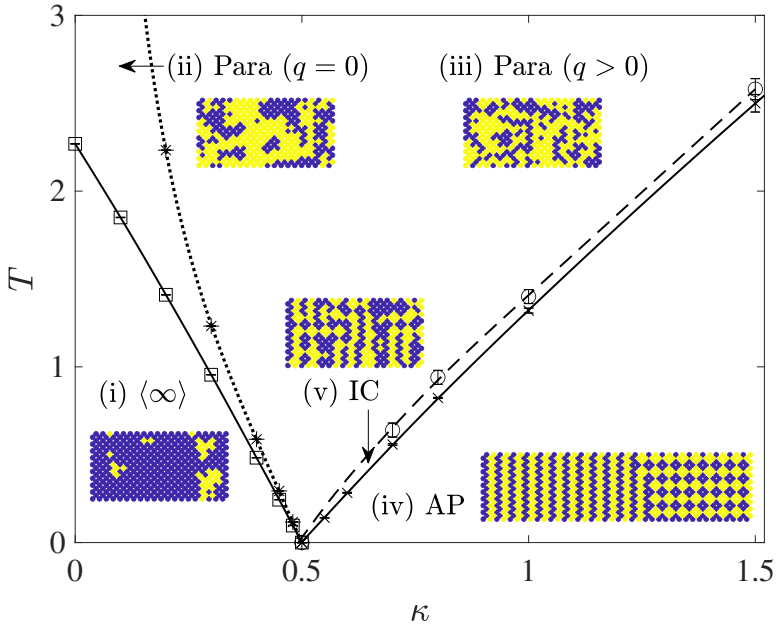

FIGURE 3.14: Phase diagram for the BNNNI model. The TM approach provides phase boundaries for the ferromagnetic $\langle\infty\rangle$-paramagnetic (squares), degenerate antiphases (AP) to IC (crosses), and paramagnetic-IC (circles) transition. The disorder line (asterisks) subdivides the paramagnetic phase into $q = 0$ and $q > 0$ modulation wavenumbers. Configuration snapshots generated by planting [33] with /TM use blue and yellow dots to denote $+1$ and -1 spins, respectively.

crossings, to the paramagnetic phase. The quantitative estimates are here fully consistent with earlier TM results [20] and the free fermion approximation [89]. An additional disorder line can be identified from the splitting of subleading eigenvalues from a pair of complex conjugates (at high T) into two distinct real numbers (at low T). Being non-critical, these two lines are only marginally affected by finite-size corrections [20]. For $\kappa > 1/2$, two transitions can be identified, $T_{c2} < T_{c1}$, as discussed in Sec. 3.3.2. Existing predictions for T_{c2} vary dramatically, but our results robustly fall between those of Ref. [59] and those of Ref. [89]. Around $\kappa = 1/2$, the TM approach suggests that the phase boundary has a finite slope on both sides of the multicritical point, thus supporting the free fermion approximation results over those of the renormalization group approach [87]. For T_{c1}, various qualitative proposals have been made [87, 88], but to the best of our knowledge no quantitative estimate

has been reported. Our results, albeit still somewhat imprecise, are consistent with the two-step melting scenario persisting over a wide range of κ and the presence of intermediate critical IC phase.

3.4 3NNI model

3.4.1 Overview

Landau and Binder determined the energetic ground state structure of the more general 3NNI model with antiferromagnetic Ising interactions [59] (see Fig. 3.11), which can be mapped onto ferromagnetic Ising interactions by flipping every other spin on the lattice. In short, while the ferromagnetic (F) phase persists for $\kappa + \kappa' < 1/2$, the ground state either follows that of the BNNNI model—4×4 checkerboard or diagonal stripes of width 2 (both denoted 4×4, for convenience)—at large κ, or that of the DNNI model—$\langle 1 \rangle$ stripes—at large κ'. At large frustration, the separation line is given by $\kappa' = 2\kappa$, and at intermediate frustration, the $\langle 2 \rangle$ phase is also a ground state. By contrast to the ANNNI model, however, the modulation can here grow along either axial directions (on a square lattice), hence the ground state is eight-fold (instead of four-fold) degenerate. The transition is further thought to be first-order—as for the 8-state Potts model—instead of continuous [34].

Interestingly, the lattice gas representation of the 3NNI model is also the two-dimensional counterpart to the Widom-Wheeler lattice microemulsion model [90] (with h corresponding to the chemical potential). Interestingly, the 3NNI model presents a $\langle 2 \rangle$ phase—a lamellar microphase in the language of Ref. [90]—as a result of the competition between DNN and BNNN interactions. We thus here concentrate on this particular regime.

3.4.2 Melting of antiphases

As shown in Fig. 3.11, the ground state configuration then depends on both κ and κ'. The model is thus expected to present different types of order-disorder transitions, as characterized by the correlation length scaling (Fig. 3.15). In parameter regimes corresponding to the ferromagnetic, $\langle 1 \rangle$ or 4×4 ground state configurations, these lengths indeed behave distinctly. Different regimes analogous to those observed in other models can further be identified (Fig. 3.15).

- In the ferromagnetic regime, ξ_1/L curves cross then kink as T increases, as they would for the thermodynamic phase transition T_c and for the disorder line crossover of the BNNNI model (the dotted line in Fig. 3.14), respectively.

- In the $\langle 1 \rangle$ regime, ξ_1/L decays monotonically and presents a single fixed point. The order of phase transition as well as the critical exponent values in the continuous transition regime also vary with the choice of (κ, κ') [34], as in the DNNI model [Fig. 3.7(a)].

- In the 4×4 regime, the ξ_1/L curves from $_/$TM plateau after the crossing, as in the BNNNI model [Fig. 3.12(b)].

The $\langle 2 \rangle$ phase of the 3NNI model, however, melts differently from that of the ANNNI model. As shown in [Fig. 3.15(d)], ξ_1/L curves cross at single point (for congruent $L \mod 4$), then decay monotonically without exhibiting any shoulder [cf. Fig. 3.1(b)]. This transition has been identified as being first-order [34, 59], but the distinction between a first-order and a Pokrovsky-Talapov transition is ambiguous in Monte Carlo simulations [59, 86]. The TM results clearly support the former over the latter.

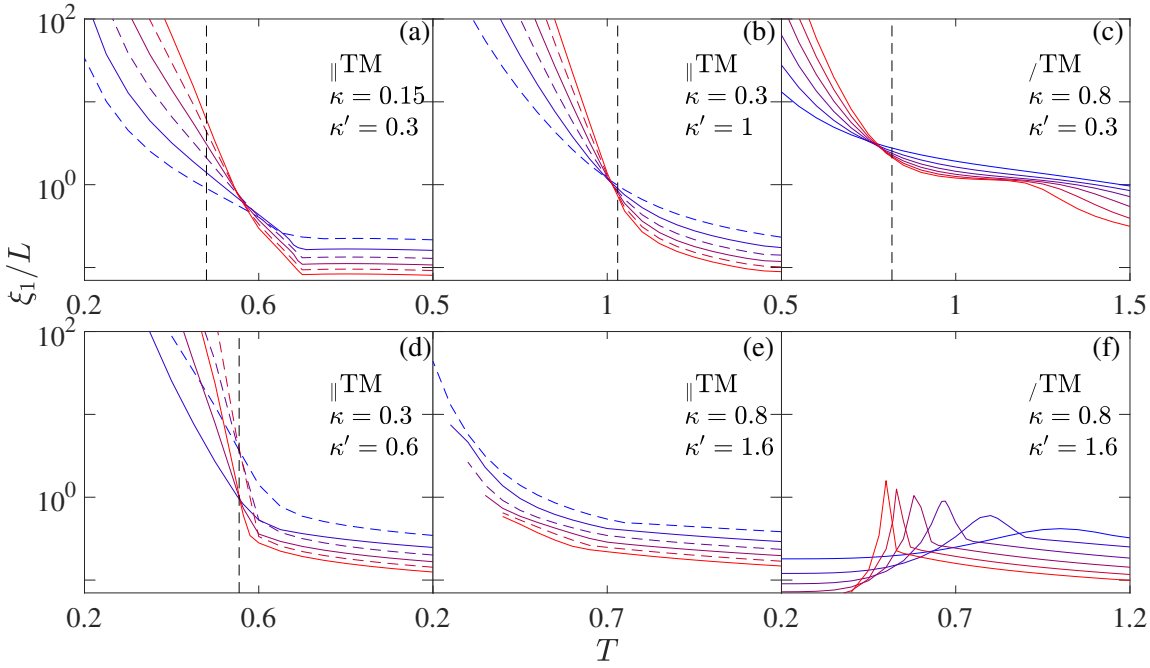

FIGURE 3.15: Correlation length scaling of the 3NNI model for different frustration parameters. For $_{\|}$TM: solid and dashed lines denote systems with $L = 8, 12, 16$ and $L = 6, 10, 14$, from blue to red, respectively. For $_{/}$TM: lines denote $L = 8, 12, ..., 28$, from blue to red, respectively. In (a-d), the ground states are ferromagnetic, $\langle 1 \rangle$, 4×4 and $\langle 2 \rangle$, respectively (See Fig. 3.11). In (e, f), the ground state is disordered. Note that results in (e) are truncated at large L and low T. Numerical instability then give complex λ_0.

3.4.3 Phase diagram for $\kappa = \kappa'/2$

As mentioned in Sec. 3.4.1, the three-dimensional version of the 3NNI model was proposed as a minimal model of microemulsions. Frustration parameters were then set to $\kappa = \kappa'/2$ in order to match the oil-water-surfactant representation [90, 91]. Interestingly, in two dimension this parameter choice results in crossing $\langle 2 \rangle$—lamellar-like—regime, and then following the $\langle 1 \rangle$–4×4 boundary, at which the system is always disordered, as frustration increases. We thus here consider the large frustration regime ($\kappa = \kappa'/2 > 1/2$). For $_{\|}$TM [Fig. 3.15(e)], ξ_1/L grows monotonically with decreasing T but no crossing is detected. Presumably ξ_1/L then diverges at a zero temperature phase transition. For $_{/}$TM [Fig. 3.15(f)], however, the ξ_1/L peak

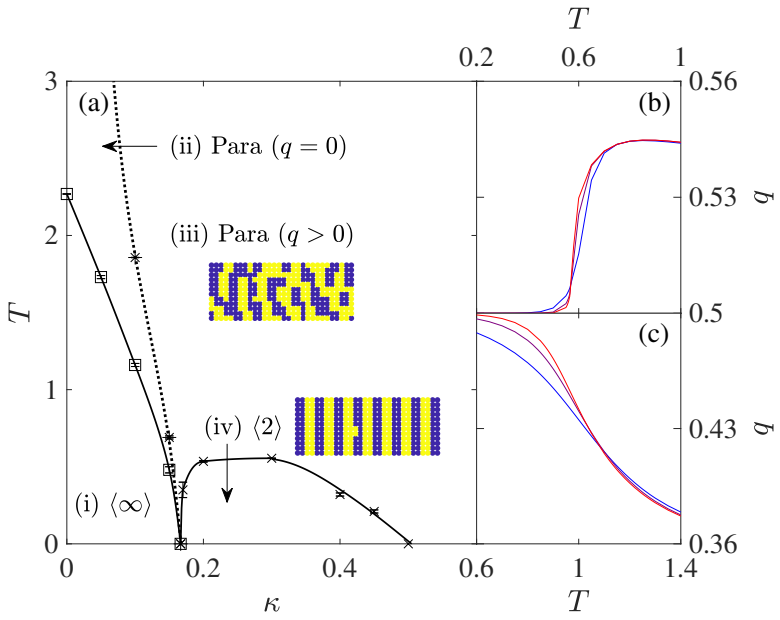

FIGURE 3.16: (a) Phase diagram for the 3NNI model for $\kappa = \kappa'/2$. The TM approach provides phase boundaries for the ferromagnetic $\langle \infty \rangle$-paramagnetic (squares), $\langle 2 \rangle$ antiphases to paramagnetic (crosses), and the disorder line (asterisks) subdivides the paramagnetic phase into $q = 0$ and $q > 0$ modulation wavenumbers. Configuration snapshots generated by planting [33] with $_{\parallel}$TM use blue and yellow dots to denote $+1$ and -1 spins, respectively. (b, c) The modulation wavenumber q given by $_{\parallel}$TM for (b) the 3NNI model with $\kappa = 0.15, \kappa' = 0.3$ and (c) ANNNI model with $\kappa = 0.6$ in $L = 8, 12, 16$, from blue to red lines.

shifts to lower T at large L, a behavior reminiscent of what happens at $\kappa = 1/2$ in the DNNI model [Fig. 3.10(c)]. Interestingly, in the limit $\kappa(= \kappa'/2) \to \infty$, the model reduces to two penetrating and decoupled DNNI antiferromagnets with $\kappa = 1/2$. The $_{\parallel}$TM and $_{/}$TM approaches for the 3NNI model are then equivalent to the $_{/}$TM and $_{\perp}$TM approaches for the DNNI model, respectively. The model is thus always disordered beyond a zero-temperature phase transition [77].

A sketch of the κ-T phase diagram (at $\kappa = \kappa'/2$) for the 3NNI model can be seen in Fig. 3.16(a). The emergence of lamellar microphases at intermediate frustration is characteristics of SALR microphase formers [24, 31, 92, 93]. Specifically, a single first-order transition bounds the $\langle 2 \rangle$ phase between $1/6 < \kappa < 1/2$. The wavenumber q along the axial direction jumps at the transition [Fig. 3.16(b)], as expected of a first-

order transition scenario. This behavior sharply contrasts with the stepwise decrease of q in the ANNNI model [Fig. 3.16(c)], which is expected to follow a square-root singularity in the thermodynamic limit [47, 48, 51]. The disordered phases in these two models are also morphologically different. In the 3NNI model, spin clusters of width 2 ($\uparrow\uparrow$) echo the dissolved modulation. For the ANNNI model, spins instead form layers of width > 2 in the vicinity of $T > T_{c1}$ [Fig. 3.3(d)], echoing the floating IC phase. In summary, the first-order scenario for the 3NNI model at $\kappa = \kappa'/2$ is reminiscent of its three-dimensional counterpart, which also exhibit a weakly first-order transition at the melting of the modulated phase [90].

4

Conclusions

We designed and implemented an efficient numerical TM algorithm for a family of next-nearest-neighbor Ising models. Combining a sparse matrix decomposition with an equivalent state transformation, the time complexity of the matrix-vector multiplication operation is of $\mathcal{O}(2^L L)$ for ${}_{\perp}$TM and ${}_{/}$TM, and $\mathcal{O}(4^L)$ for ${}_{\parallel}$TM; the space complexity of the algorithm is of $\mathcal{O}(2^L/L)$ for ${}_{\perp}$TM and ${}_{/}$TM, and $\mathcal{O}(4^L/L)$ for ${}_{\parallel}$TM. The space complexity (and the time complexity for ${}_{\parallel}$TM) has thus improved by $1/L$ compared to previous approaches.

Using this numerical TM approach, we have studied a series of two-dimensional frustrated Ising models in order to resolve various long-standing questions about their phase behavior. For the ANNNI model, we obtained the complete phase diagram for $h = 0$, and identified the incommensurate lamellar phase and its reentrance for $h \neq 0$. For the DNNI model, the TM results confirmed the location of the transition in the limiting case $T_{\mathrm{c}}(\kappa = 1/2) = 0$, and support and distinguish the weakly first-order transition scenario for $\kappa^{\dagger} < \kappa < 1/2$ and for $1/2 < \kappa < \kappa^{*}$. For the BNNNI model, a strong signature of the critical IC phase has been captured, even though its upper boundary remains imprecise. For the 3NNI model, the lamellar modulated regime

has been shown to melt with a single first-order transition, in contrast to that of the ANNNI model. Combining these findings provides a systematic overview of modulated phase formation, and the high-accuracy results benchmark other theoretical and numerical approaches.

Nevertheless, the numerical TM method still suffers from an insufficiently wide range of system sizes under certain circumstances, such as determining T_{c1} for the BNNNI model. Some of these problems might be resolved, in time, with ever improving computers architecture and by relaxing the exactness, such as by using inexact eigensolvers [8] or truncated configuration representations as in the DMRG approach [9, 48]. In the mean time, the approach could be extended to other lattice models such as spin-1 and Potts models. The approach could also inspire the development of adapted eigensolver for similarly structured matrices.

Bibliography

[1] Y. Saad, "Numerical methods for large eigenvalue problems: revised edition," (SIAM, 2011) Chap. Preface.

[2] C. Lanczos, Journal of Research of the National Bureau of Standards **45**, 255 (1950).

[3] W. E. Arnoldi, Quarterly of applied mathematics **9**, 17 (1951).

[4] R. B. Lehoucq, D. C. Sorensen, and C. Yang, *ARPACK users' guide: solution of large-scale eigenvalue problems with implicitly restarted Arnoldi methods* (SIAM, 1998).

[5] G. L. Sleijpen and H. A. Van der Vorst, SIAM review **42**, 267 (2000).

[6] G. H. Booth, A. J. Thom, and A. Alavi, The Journal of chemical physics **131**, 054106 (2009).

[7] L.-H. Lim and J. Weare, SIAM Review **59**, 547 (2017).

[8] Z. Wang, *Efficient Algorithms for High-Dimensional Eigenvalue Problems*, Ph.D. thesis, Duke University (2020).

[9] T. Nishino, Journal of the Physical Society of Japan **64**, 13 (1995).

[10] S. R. White and R. L. Martin, The Journal of chemical physics **110**, 4127 (1999).

[11] G. K.-L. Chan and S. Sharma, Annual review of physical chemistry **62**, 465 (2011).

[12] H. A. Kramers and G. H. Wannier, Physical Review **60**, 252 (1941).

[13] R. J. Baxter, *Exactly solved models in statistical mechanics* (Academic Press, 1982).

[14] S. G. Brush, Reviews of modern physics **39**, 883 (1967).

[15] H. Nishimori, *Statistical physics of spin glasses and information processing: an introduction*, 111 (Clarendon Press, 2001).

[16] Z. Wang, A. Marandi, K. Wen, R. L. Byer, and Y. Yamamoto, Physical Review A **88**, 063853 (2013).

[17] F. Krzakala, F. Ricci-Tersenghi, L. Zdeborova, R. Zecchina, E. W. Tramel, and L. F. Cugliandolo, *Statistical physics, optimization, inference, and message-passing algorithms* (Oxford University Press Oxford, 2016).

[18] W. Pesch and J. Kroemer, Zeitschrift für Physik B Condensed Matter **59**, 317 (1985).

[19] P. D. Beale, P. M. Duxbury, and J. Yeomans, Physical Review B **31**, 7166 (1985).

[20] J. Oitmaa, M. T. Batchelor, and M. N. Barber, Journal of Physics A: Mathematical and General **20**, 1507 (1987).

[21] S. Jin, A. Sen, W. Guo, and A. W. Sandvik, Physical Review B **87**, 144406 (2013).

[22] Y. Hu and P. Charbonneau, Physical Review B **103**, 094441 (2021).

[23] F. Sciortino, S. Mossa, E. Zaccarelli, and P. Tartaglia, Physical review letters **93**, 055701 (2004).

[24] Y. Zhuang, K. Zhang, and P. Charbonneau, Physical review letters **116**, 098301 (2016).

[25] M. E. Fisher and W. Selke, Physical Review Letters **44**, 1502 (1980).

[26] A. K. Chandra and S. Dasgupta, Journal of Physics A: Mathematical and Theoretical **40**, 6251 (2007).

[27] T. Shirakura, F. Matsubara, and N. Suzuki, Physical Review B **90**, 144410 (2014).

[28] F. Matsubara, T. Shirakura, and N. Suzuki, Physical Review B **95**, 174409 (2017).

[29] M. J. Godfrey and M. A. Moore, Physical Review E **91**, 022120 (2015).

[30] J. F. Robinson, M. J. Godfrey, and M. A. Moore, Physical Review E **93**, 032101 (2016).

[31] Y. Hu and P. Charbonneau, Soft Matter **14**, 4101 (2018).

[32] Y. Hu, L. Fu, and P. Charbonneau, Molecular Physics **116**, 3345 (2018).

[33] Y. Hu and P. Charbonneau, arXiv preprint (2020), arXiv:2009.11194 .

[34] R. Liu, W. Zhuo, S. Dong, X. Lu, X. Gao, M. Qin, and J.-M. Liu, Physical Review E **93**, 032114 (2016).

[35] L. N. Trefethen and D. Bau III, *Numerical linear algebra*, Vol. 50 (SIAM, 1997).

[36] P. Virtanen, R. Gommers, T. E. Oliphant, M. Haberland, T. Reddy, D. Cournapeau, E. Burovski, P. Peterson, W. Weckesser, J. Bright, *et al.*, Nature methods **17**, 261 (2020).

[37] Y. Qiu, "Spectralib (sparse eigenvalue computation toolkit as a redesigned ARPACK [4])," (2020).

[38] A. Cantoni and P. Butler, Linear Algebra and its Applications **13**, 275 (1976).

[39] H. W. J. Blöte and M. P. Nightingale, Physica A: Statistical Mechanics and its Applications **112**, 405 (1982).

[40] W. Selke, Zeitschrift für Physik B Condensed Matter **43**, 335 (1981).

[41] M. Beccaria, M. Campostrini, and A. Feo, Physical Review B **73**, 052402 (2006).

[42] M. Beccaria, M. Campostrini, and A. Feo, Physical Review B **76**, 094410 (2007).

[43] J. Villain and P. Bak, Journal de Physique **42**, 657 (1981).

[44] J. Oitmaa, Journal of Physics A: Mathematical and General **18**, 365 (1985).

[45] A. Finel and D. de Fontaine, Journal of statistical physics **43**, 645 (1986).

[46] M. A. S. Saqi and D. S. McKenzie, Journal of Physics A: Mathematical and General **20**, 471 (1987).

[47] W. Selke, Physics Reports **170**, 213 (1988).

[48] R. Derian, A. Gendiar, and T. Nishino, Journal of the Physical Society of Japan **75**, 114001 (2006).

[49] W. Selke and M. E. Fisher, Zeitschrift für Physik B Condensed Matter **40**, 71 (1980).

[50] J. M. Kosterlitz and D. J. Thouless, Journal of Physics C: Solid State Physics **6**, 1181 (1973).

[51] A. Sato and F. Matsubara, Physical Review B **60**, 10316 (1999).

[52] E. Rastelli, S. Regina, and A. Tassi, Physical Review B **81**, 094425 (2010).

[53] T. Shirahata and T. Nakamura, Physical Review B **65**, 024402 (2001).

[54] H. L. Richards, M. A. Novotny, and P. A. Rikvold, Physical Review B **48**, 14584 (1993).

[55] V. Privman, *Finite size scaling and numerical simulation of statistical systems* (World Scientific, 1990).

[56] A. E. Ferdinand and M. E. Fisher, Physical Review **185**, 832 (1969).

[57] J. Salas, Journal of Physics A: Mathematical and General **34**, 1311 (2001).

[58] P. Nightingale, Journal of Applied Physics **53**, 7927 (1982).

[59] D. P. Landau and K. Binder, Physical Review B **31**, 5946 (1985).

[60] V. L. Pokrovsky and A. L. Talapov, Physical Review Letters **42**, 65 (1979).

[61] B. Nienhuis, H. J. Hilhorst, and H. W. J. Blote, Journal of Physics A: Mathematical and General **17**, 3559 (1984).

[62] P. M. Duxbury, J. Yeomans, and P. D. Beale, Journal of Physics A: Mathematical and General **17**, L179 (1984).

[63] M. N. Barber and P. M. Duxbury, Journal of Physics A: Mathematical and General **14**, L251 (1981).

[64] J. Stephenson, Canadian Journal of Physics **48**, 1724 (1970).

[65] I. Peschel and V. J. Emery, Zeitschrift für Physik B Condensed Matter **43**, 241 (1981).

[66] A. Ciach, J. Pękalski, and W. T. Góźdź, Soft Matter **9**, 6301 (2013).

[67] P. Rujan, W. Selke, and G. V. Uimin, Zeitschrift für Physik B Condensed Matter **53**, 221 (1983).

[68] A. I. Guerrero, D. A. Stariolo, and N. G. Almarza, Physical Review E **91**, 052123 (2015).

[69] R. A. dos Anjos, J. R. Viana, and J. R. de Sousa, Physics Letters A **372**, 1180 (2008).

[70] A. Kalz, A. Honecker, and M. Moliner, Physical Review B **84**, 174407 (2011).

[71] S. Jin, A. Sen, and A. W. Sandvik, Physical Review Letters **108**, 045702 (2012).

[72] H. Li and L.-P. Yang, arXiv preprint (2021), arXiv:2103.09464 .

[73] A. Bobák, T. Lučivjanskỳ, M. Borovskỳ, and M. Žukovič, Physical Review E **91**, 032145 (2015).

[74] Y. Boughaleb, M. Nouredine, M. Snina, R. Nassif, and M. Bennai, Physics Research International **2010** (2010), 10.1155/2010/284231.

[75] M. Ramazanov, A. Murtazaev, and M. Magomedov, Solid State Communications **233**, 35 (2016).

[76] R. Timmons and K. De?Bell, Canadian Journal of Physics **96**, 912 (2018).

[77] D. P. Landau, Physical Review B **21**, 1285 (1980).

[78] J. Morán-López, F. Aguilera-Granja, and J. Sanchez, Physical Review B **48**, 3519 (1993).

[79] A. Kalz, A. Honecker, S. Fuchs, and T. Pruschke, The European Physical Journal B **65**, 533 (2008).

[80] A. Kalz, A. Honecker, S. Fuchs, and T. Pruschke, in *Journal of Physics: Conference Series*, Vol. 145 (IOP Publishing, 2009) p. 012051.

[81] S.-Y. Kim, Physical Review E **81**, 031120 (2010).

[82] J. Oitmaa, Journal of Physics A: Mathematical and General **14**, 1159 (1981).

[83] M. P. Nightingale, Physica A: Statistical Mechanics and its Applications **83**, 561 (1976).

[84] P. Charbonneau and M. Tarzia, arXiv preprint (2021), arXiv:2103.14450 .

[85] J. H. Lee, H. S. Song, J. M. Kim, and S.-Y. Kim, Journal of Statistical Mechanics: Theory and Experiment **2010**, P03020 (2010).

[86] M. J. Velgakis and J. Oitmaa, Journal of Physics A: Mathematical and General **21**, 547 (1988).

[87] M. Aydin and M. C. Yalabik, Journal of Physics A: Mathematical and General **22**, 85 (1989).

[88] M. Aydin and M. C. Yalabik, Journal of Physics A: Mathematical and General **22**, 3981 (1989).

[89] S. Dasgupta, Journal of Physics A: Mathematical and General **24**, 1017 (1991).

[90] K. A. Dawson, M. D. Lipkin, and B. Widom, The Journal of chemical physics **88**, 5149 (1988).

[91] B. Widom, The Journal of chemical physics **84**, 6943 (1986).

[92] N. G. Almarza, J. Pękalski, and A. Ciach, The Journal of Chemical Physics **140**, 164708 (2014).

[93] Y. Zhuang and P. Charbonneau, The Journal of Physical Chemistry B **120**, 7775 (2016).